Wang, H., He, Y., Lühr, H., Kistler, L., Saikin, A., Lund, E., Ma, S. (2019): Storm Time EMIC Waves Observed by Swarm and Van Allen Probe Satellites. - *Journal of Geophysical Research*, *124*, 1, pp. 293—312.

DOI: http://doi.org/10.1029/2018JA026299

JGR Space Physics

RESEARCH ARTICLE
10.1029/2018JA026299

Storm Time EMIC Waves Observed by Swarm and Van Allen Probe Satellites

Hui Wang[1,2], Yangfan He[1], Hermann Lühr[3], Lynn Kistler[2], Anthony Saikin[2], Eric Lund[2], and Shuying Ma[1]

[1]Department of Space Physics, School of Electronic Information, Wuhan University, Hubei, China, [2]Department of Physics and Space Science Center (EOS), University of New Hampshire, Durham, NH, USA, [3]GFZ German Research Center for Geosciences, Potsdam, Germany

Key Points:
- EMIC waves are not detected in the magnetosphere and ionosphere around the *SYM-H* minimum
- Both ionospheric wave frequency and power are higher in the summer hemisphere than in the winter hemisphere
- Waves are confined to an MLT interval of less than 5 hr and have a duration of less than 186 min from coordinated VAP-SWARM observations

Correspondence to:
H. Wang,
h.wang@whu.edu.cn

Citation:
Wang, H., He, Y. F., Lühr, H., Kistler, L., Saikin, A., Lund, E., & Ma, S. (2019). Storm time EMIC waves observed by Swarm and Van Allen Probe satellites. *Journal of Geophysical Research: Space Physics*, *124*, 293–312. https://doi.org/10.1029/2018JA026299

Received 14 NOV 2018
Accepted 4 JAN 2019
Accepted article online 10 JAN 2019
Published online 25 JAN 2019

Abstract The temporal and spatial evolution of electromagnetic ion cyclotron (EMIC) waves during the magnetic storm of 21–29 June 2015 was investigated using high-resolution magnetic field observations from Swarm constellation in the ionosphere and Van Allen Probes in the magnetosphere. Magnetospheric EMIC waves had a maximum occurrence frequency in the afternoon sector and shifted equatorward during the expansion phase and poleward during the recovery phase. However, ionospheric waves in subauroral regions occurred more frequently in the nighttime than during the day and exhibited less obvious latitudinal movements. During the main phase, dayside EMIC waves occurred in both the ionosphere and magnetosphere in response to the dramatic increase in the solar wind dynamic pressure. Waves were absent in the magnetosphere and ionosphere around the minimum *SYM-H*. During the early recovery phase, He^+ band EMIC waves were observed in the ionosphere and magnetosphere. During the late recovery phase, H^+ band EMIC waves emerged in response to enhanced earthward convection during substorms in the premidnight sector. The occurrence of EMIC waves in the noon sector was affected by the intensity of substorm activity. Both ionospheric wave frequency and power were higher in the summer hemisphere than in the winter hemisphere. Waves were confined to an MLT interval of less than 5 hr with a duration of less than 186 min from coordinated observations. The results could provide additional insights into the spatial characteristics and propagation features of EMIC waves during storm periods.

1. Introduction

It is important to understand the spatial and temporal variations of electromagnetic ion cyclotron (EMIC) waves, as they play an important role in controlling particle dynamics in the magnetosphere. They can induce transverse energization of ions and cause their subsequent outflow (e.g., Bortnik et al., 2010), precipitate ions in the ring current via resonant pitch angle scattering (e.g., Jordanova et al., 2001), and cause precipitation of ultrarelativistic electrons from the radiation belt into the atmosphere via resonant wave-particle interactions (e.g., Thorne & Kennel, 1971). EMIC waves are generated by energetic (10–100 keV) and anisotropic (perpendicular temperature > parallel temperature) ions that overlap with cold dense plasma populations. The energetic populations provide the free energy necessary to facilitate the EMIC wave instability (Cornwall, 1965; Rauch & Roux, 1982), while the cold dense plasma serves to increase the convective growth rates (Horne & Thorne, 1993; Rauch & Roux, 1982; Young et al., 1981).

EMIC waves are typically observed within the range of 0.1 to 5 Hz (Rauch & Roux, 1982). The cold plasma population also dictates at which frequencies EMIC wave activity can be excited and observed. Varying the concentration and composition of the cold plasma (between hydrogen [H^+], helium [He^+], and oxygen [O^+]) determines in which frequency band EMIC wave excitation can occur (Kozyra et al., 1984; Saikin et al., 2018). The H^+ band lies below the gyrofrequency of H^+ and above the gyrofrequency of He^+. The He^+ band lies between the gyrofrequency of He^+ and O^+. The O^+ band lies below the gyrofrequency of O^+. EMIC waves can propagate along the magnetic field lines, and ionospheric Pc1/2 pulsations are commonly related to EMIC waves generated in the magnetosphere.

Over the years, numerous statistical studies on the distribution and occurrence rates of EMIC waves in the magnetosphere have been performed, using data from the following satellites: Active Magnetospheric Particle Tracer Explorer/Charge Composition Explorer (Anderson et al., 1992; Keika et al., 2013), Akebono

(e.g., Kasahara et al., 1992), Time History of Events and Macroscale Interactions during Substorms (e.g., Min et al., 2012; Usanova et al., 2012), Cluster (Allen et al., 2015, 2016), Geostationary Operational Environmental Satellite (e.g., K.-H. Kim et al., 2016; Park et al., 2016), Combined Release and Radiation Effects Satellite (CRRES; e.g., Halford et al., 2010; Min et al., 2012; Meredith et al., 2014), Dynamic Explorer 1 (Erlandson & Ukhorskiy, 2001), Van Allen Probes (VAPs; Saikin et al., 2015; D. Wang et al., 2015; Yu et al., 2015), and Magenetospheric Multiscale mission (X. Y. Wang et al., 2017). Ionospheric EMIC waves have been statistically studied using data from the Magnetic Field Satellite, Freja, Dynamic Explorer 2, Challenging Minisatellite Payload, and Swarm satellites (e.g., Erlandson & Anderson, 1996; Iyemori & Hayashi, 1989; H. Kim et al., 2018; Mursula et al., 1994; Park et al., 2013). These studies found that the source regions of EMIC waves varied over a wide range of magnetic local times (MLTs) from 03:00 to 20:00 MLT and over the L shells from 2 to 13 R_E, which correspond to the range of invariant latitudes (ILat) from 45° (midlatitudes) to 74° (auroral zone). Waves in the three frequency bands (H^+, He^+, and O^+) were found to exhibit peaks at different MLTs and in different L shells (latitudes). Differences in the statistical results might be due to different spatial swaths covered by the various satellite missions.

It remains controversial whether EMIC waves occur more frequently during the main phase or the recovery phase of geomagnetic storms. During the main phase, the injection of high-energy ions from the plasma sheet increases, which can provide more free energy for the generation of EMIC waves (Fraser & Nguyen, 2001). By using data from both the Freja satellite and Finnish ground-based magnetometers during 2–8 April 1993, Bräysy et al. (1998) found O^+ band EMIC waves during a limited period of about 7 hr in the late main phase. Blum et al. (2009) found a higher occurrence of enhanced EMIC waves in the main phase of a storm with or without net losses of relativistic electrons by using observations from the Los Alamos National Laboratory Magnetospheric plasma Analyzer. By using observations from the CRRES mission ($L < 6.3R_E$), Halford et al. (2010) found that the majority of storm time EMIC waves occurred during the main phase, whereas a minority occurred during the recovery phase. The mean location of occurrence from the CRRES mission was $L = 6R_E$ and MLT = 15:00, which suggested that EMIC waves were generated when the ring current and plasmasphere or plasma plume particles overlapped.

During the recovery phase, there may be more regions of overlap between the ring current and the plasmasphere, which is favorable for the generation of EMIC waves (Fraser & Nguyen, 2001). Engebretson, Lessard, et al. (2008) found that EMIC waves were absent during the main phase and early recovery phase of storms during two storms in 2005 by using ground-based observations. This result was supported by Engebretson, Posch, et al. (2008) by the inclusion of observations from Space Technology 5 satellites. Using observations from geosynchronous satellites, Fraser et al. (2010) found that 29% of wave events occurred during the main phase in comparison with 71% during the recovery phase. By using VAP data ($L < 5.8R_E$), Saikin et al. (2016) examined the correlation between the occurrence of EMIC waves and geomagnetic conditions, as well as the dynamic pressure of the solar wind. They found that waves were observed more often during the recovery phase than during the main phase, which was consistent with findings by D. Wang et al. (2016). Halford et al. (2016) considered how the occurrence of waves varied with the phase of the storms and found that EMIC waves occurring during the recovery phase have plasma and wave characteristics that were more similar to those found during quiet conditions than to those observed during the main phase. Using 3 years of Swarm A observations in the ionosphere, H. Kim et al. (2018) found that EMIC waves exhibited some correlation with geomagnetic activity, with a tendency to occur during the late recovery phase of the storms at low Earth orbit. However, their work did not mention differences by hemisphere/local time or the three wave bands, which are the objectives in the present study. Ground-based studies have found that EMIC waves were observed more frequently on multiple days after the disturbance storm time index of an isolated storm reached a minimum (e.g., Bortnik et al., 2008).

Previous works have investigated the different features of three wave bands in the high- and low-L shell regions of the magnetosphere separately but not in the ionosphere (Keika et al., 2013; Min et al., 2012; Meredith et al., 2014; Saikin et al., 2015; Yu et al., 2015). By using nearly 4.5 years of magnetic field data from Active Magnetospheric Particle Tracer Explorer/Charge Composition Explorer satellites during storm periods, Keika et al. (2013) found that the region of peak occurrence of H^+ and He^+ EMIC waves was in the outer magnetosphere at approximately $L > 7R_E$. H^+ band waves peaked in the daytime sector, which was attributed to the compression of the magnetosphere, whereas He^+ band waves mostly occurred in the afternoon sector, which was correlated with the injection of hot ions from the plasma sheet. From Time History of Events and Macroscale Interactions during Substorms observations, Min et al. (2012) reported

the occurrence of dawn-centered H^+ band waves in the higher L shells, but there was a decrease in the occurrence of H^+ band waves around 09:00–11:00 MLT from 6.5 to 14 R_E. By using CRRES observations, Meredith et al. (2014) reported that the regions of peak occurrence of H^+ and He^+ band waves were in the afternoon sector in the inner magnetosphere ($L < 7R_E$). This was in agreement with findings by Saikin et al. (2015) based on VAPs observations. Most O^+ band wave events occurred inside the plasmapause and around 06:00–13:00 MLT (Saikin et al., 2015; Yu et al., 2015). In low-L shell regions ($L = 1.5R_E$) Kasahara et al. (1992) found that the region of peak occurrence of H^+ and He^+ band EMIC waves was in the evening sector (16:00–20:00 MLT). By using a ray tracing technique, they showed that H^+ band waves were more easily generated in lower L shell region than He^+ band waves.

The propagation features of EMIC waves have been studied using ground-based and satellite observations and theoretical analysis (e.g., Engebretson, Lessard, et al., 2008; Engebretson, Posch, et al., 2008; Engebretson et al., 2015; Johnson & Cheng, 1999; H. Kim et al., 2011; K.-H. Kim et al., 2016; Lund & LaBelle, 1997; Morley et al., 2009; Perraut et al., 1984; Rauch & Roux, 1982). Coordinated observations of both the magnetosphere and the ionosphere are few in the literature. Because the ionosphere is a region of incidence of EMIC waves, a combined study of both the ionosphere and the magnetosphere could help to better understand the spatial propagation feature of EMIC waves. Perraut et al. (1984) reported significant correlations between waves in the magnetosphere and on the ground (about 50% of events reached the ground), which suggested that waves propagated from the magnetosphere to the ground. During the main phase of storms, wave events were absent both on the ground (Engebretson, Lessard, et al., 2008) and in the magnetosphere (Engebretson, Posch, et al., 2008). Engebretson et al. (2015) showed that EMIC waves were observed across a broad range of local times and L shells in both VAP and ground observations, and these were associated with strong magnetospheric compression. Using a ray tracing technique, Rauch and Roux (1982) found that a left-handed polarized EMIC wave would be reflected at the location of Buchsbaum resonance (or frequency of bi-ion). On the basis of a full-wave analysis, Johnson and Cheng (1999) showed that strong mode coupling could occur near the locations of the He^+/O^+ resonance, which would allow equatorial EMIC waves to change their polarization and propagate to the ground. Using a 2D full-wave code, E.-H. Kim and Johnson (2016) confirmed that polarization reversals occurred at the crossover frequency, and a wave with right-handed polarization could thus propagate to the inner magnetosphere.

The Swarm constellations provide us with an opportunity to study the properties of ionospheric EMIC waves during storm main and recovery phases. The Swarm satellites cover a wide range of L shells (latitudes) at a roughly constant MLT and traverse the wave region rather quickly (i.e., they have a short orbital period). This makes it possible to examine the latitudinal structure of a wave within a confined MLT sector and enables almost simultaneous resolution of hemispheric differences using a single spacecraft. The Multisatellite Swarm configurations can provide additional insights into the spatial characteristics of EMIC waves. The Swarm A and Swarm C satellites and the Swarm B satellite are separated by a MLT interval of about 2 hr, which allows us to simultaneously compare storm time variations in EMIC waves in different local time sectors. As far as we know, such a comprehensive analysis of the properties of the storm time ionospheric EMIC waves in both hemispheres and at different local times has not been performed. Simultaneous observations of EMIC waves in both the magnetosphere and ionosphere by the VAPs and the Swarm constellation are also presented, and these are quite scarce in the literature. The present work could provide additional insights into the spatial characteristics and propagation features of EMIC waves during storm periods.

This paper is organized as follows. The satellite missions and data processing methods are described in section 2. Section 3 presents the results of our study of EMIC waves during geomagnetic storms. Section 4 comprises a discussion of our main results, and section 5 presents our final conclusions.

2. Data and Methods

2.1. Swarm Mission

The European Space Agency's Swarm satellites were launched into near-polar orbits with an inclination of 87.5° at an altitude of about 500 km and an orbital period of about 93 min. They reached their final constellation on 15 April 2014. Swarm A and Swarm C orbit side by side with a longitudinal separation of 1.4° at an altitude of 460 km. Swarm B orbits at about 520 km with a higher inclination. In this study we utilized high-resolution vector magnetic field data sampled at 50 Hz with an accuracy of 0.01 nT from all three satellites. During the magnetic storm of 21–29 June 2015, Swarm A and Swarm C were mainly located in the prenoon and premidnight sectors (around 10:30 and 22:30 MLT), whereas Swarm B was in the afternoon

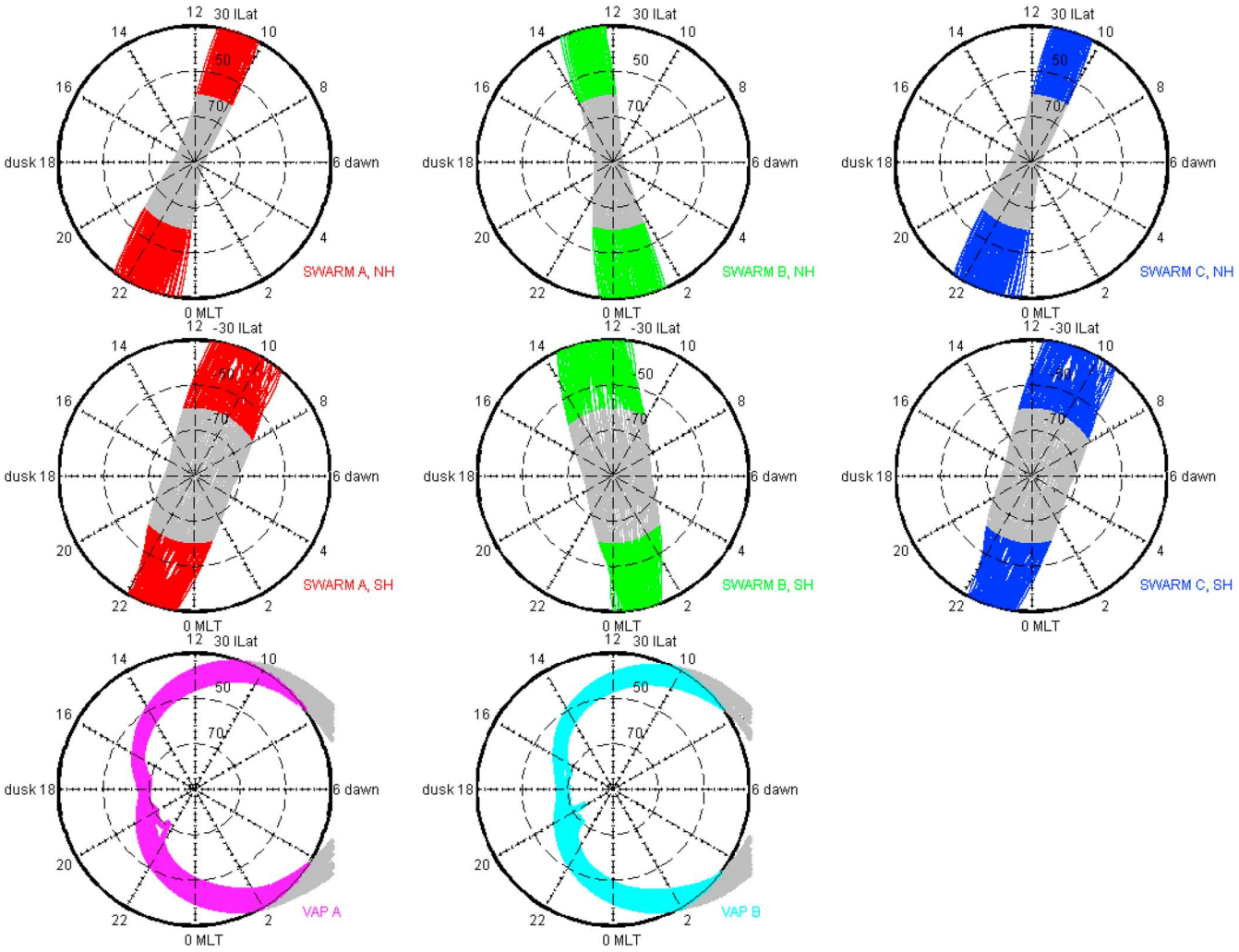

Figure 1. Trajectories of Swarms A, B, and C and ionospheric footprints of VAPs A and B during the storm periods in the invariant latitude versus magnetic local time coordinates. The regions where EMIC waves can be detected are colored in red, green, blue, magenta, and cyan for Swarms A, B, and C and VAPs A and B, respectively. The concentric circles represent 30°, 50°, and 70° ILAT, from outer to inner. Swarms A and C are in the prenoon and premidnight sectors at 460-km altitude, and Swarm B is in the afternoon and postmidnight sectors at a 520-km altitude. VAPs A and B orbit at higher latitudes in the afternoon and midnight sectors and at lower latitudes in the morning and prenoon sectors, where EMIC waves are rarely detected. VAP = Van Allen Probe; EMIC = electromagnetic ion cyclotron; ILat = invariant latitudes; MLT = magnetic local time; NH = Northern Hemisphere; SH = Southern Hemisphere.

and postmidnight sectors (13:00 and 01:00 MLT). The orbit segments of Swarm A, Swarm B, and Swarm C during storm periods in both the Northern Hemisphere (top row) and the Southern Hemisphere (middle row) are shown in Figure 1 in the ILat versus MLT coordinate system. The regions where EMIC waves were possibly detected are colored in red, green, and blue for Swarm A, Swarm B, and Swarm C, respectively (The same color scheme is used in the following). In the following description, where not specifically defined, the term latitude refers to ILat. The orbit of Swarm C is similar to Swarm A. The hemispheric differences in local time coverage between the orbits can be attributed to the difference in the offset between the geographic and geomagnetic poles in the two hemispheres.

To determine the background magnetic field, the 50-Hz magnetic field data were filtered using a Savitzky-Golay smoothing filter with a moving window of 30 × 50 data points and a second-order polynomial, a method also used by H. Kim et al. (2018). The background magnetic field was subtracted from the original 50-Hz data to determine the fluctuating field. The fluctuating field was then expressed in the field-aligned coordinate system, in which the $\vec{z}$ axis is parallel to the background magnetic field lines, $\vec{y}$ is defined as $\vec{z}\times\vec{r}$, where $\vec{r}$ is the radial vector from the Earth's center to the satellite location, and $\vec{x}$ corresponds to $\vec{y}\times\vec{z}$. The fluctuating field data were processed via the fast Fourier transform technique, and the power,

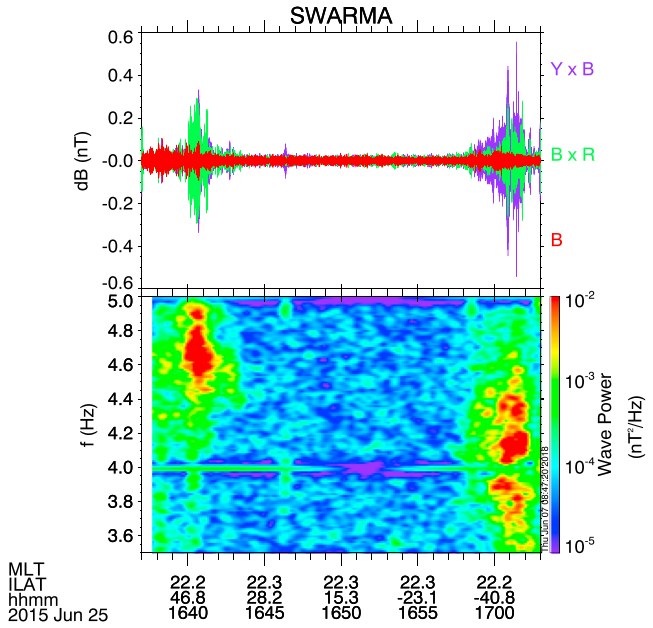

Figure 2. Stacked plot of Swarm A VFM (Vector Field Magnetometer) data from 16:35 to 17:05 UT on 25 June 2015. (top) The high-pass magnetic field component in the mean-field-aligned coordinates. The $\vec{z}$ is along the background magnetic field; $\vec{y}$ is defined as $\vec{z} \times \vec{r}$, where $\vec{r}$ is the radial vector from the Earth's center to the satellite location; and $\vec{x}$ corresponds to $\vec{y} \times \vec{z}$. The background magnetic field has been subtracted (see text for details). Swarm A is descending from the northern auroral region to the southern auroral region. (bottom) The vertical axis shows frequency from 3.5 to 5 Hz. Wave power is color coded; see color bar on the right, which is in units of square nanoteslas per hertz. Two examples of Pc1 wave events can be detected in northern and southern midlatitudes. The maximum power densities can be found at 16:41 and 17:01 UT, respectively. MLT = magnetic local time; ILat = invariant latitudes.

normal angle, and ellipticity of waves were calculated using a method similar to that described by Allen et al. (2015). Plots of Swarm data were generated for each descending and ascending orbit, and EMIC wave events were identified visually. We chose the lower and upper frequency, limits of 0.1 and 25 Hz, respectively; the gyrofrequency of O^+ in the magnetosphere is far higher than 0.1 Hz, and the gyrofrequency of H^+ is lower than 25 Hz under the investigation conditions.

An example wave spectrogram is shown in Figure 2. The top panel shows the temporal variations of the fluctuating magnetic field in the field-aligned coordinate system as observed by Swarm A from 16:37 to 17:03 universal time (UT) on 25 June 2015. The satellite was in a descending orbit traversing from north to south. It was in the premidnight sector at approximately 22:00 MLT. The bottom panel of Figure 2 shows the wave power spectral density as a function of frequency and UT. The MLT and ILat values are shown together with the UT. The detection of wave events at auroral latitudes is impossible owing to the stronger signal associated with the auroral field-aligned currents (data not shown). EMIC wave events were detected in the premidnight sector in both subauroral regions, with a greater frequency in the Northern Hemisphere than the Southern Hemisphere. These EMIC waves occurred during the storm recovery phase. In a similar way, EMIC waves were identified in both subauroral regions (from 30° to 60° and from −30° to −60° ILat) separately by Swarms A (19 events in the Northern Hemisphere and 17 events in the Southern Hemisphere), Swarm B (13 events in the Northern Hemisphere and 12 events in the Southern Hemisphere), and Swarm C (19 events in the Northern Hemisphere and 17 events in the Southern Hemisphere). The waves in equatorial regions were related to plasma bubbles (Lühr, Park, et al., 2014; Lühr, Xiong, et al., 2014) and hence were not studied in the present work. For each event, the UT, ILat, MLT, and ellipticity values for the maximum power density of the EMIC waves were recorded. We then did an analysis of these features of the waves.

2.2. VAP Mission

The twin VAPs (formerly referred to as the Radiation Belt Storm Probes) were launched by NASA in late August 2012 to investigate radiation belt dynamics. The apogee and perigee of their orbits is nearly 5.8 R_E and 1.1 R_E, respectively. Both probes have an orbital period of 9 hr and follow a low-inclination (10°) highly elliptical orbit. The perigee-apogee line precesses in local time at a rate of 210° per year. In this study, we

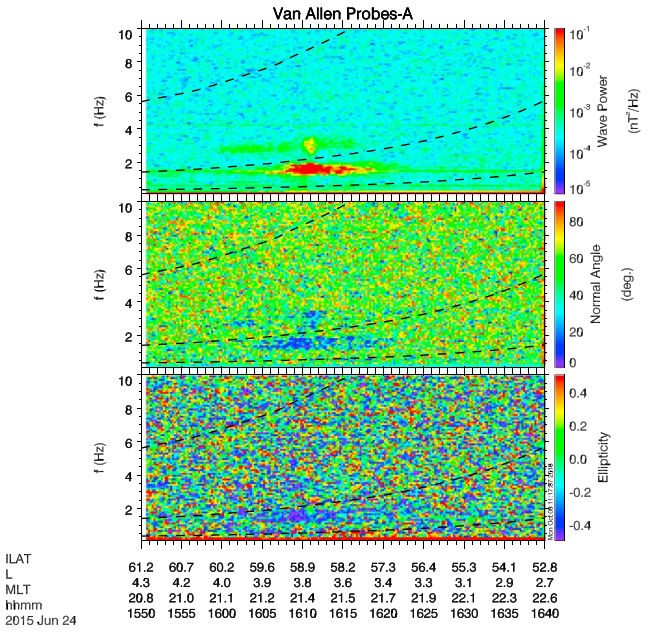

Figure 3. One example of EMIC wave events observed by Van Allen Probe A at 15:50–16:40 UT on 24 June 2015. From top to bottom are wave power density, normal angle, and ellipticity, respectively. The dashed black lines plot the local gyrofrequency of H^+, He^+, and O^+ ions. The maximum power density can be found at 16:11 and 16:10 UT for the high and low band, respectively. EMIC = electromagnetic ion cyclotron; ILat = invariant latitudes; MLT = magnetic local time.

utilized magnetometer data from the Electric and Magnetic Field Instrument Suite and Integrated Science on board VAPs A and B (Kletzing et al., 2013). During the storm of 21–29 June 2015, the apogees of the VAPs were in the dusk sector, and the perigees were in the dawn sector. Figure 1 (bottom row) shows the ionospheric footprints of VAP A and VAP B. The regions where it is possible to detect EMIC waves are shown in magenta and cyan for VAP A and VAP B, respectively. The locations of the VAPs were magnetically mapped to the ionospheric altitude by tracing field lines in the Tsyganenko 1996 model (Tsyganenko, 1995; 1996).

We utilized a 10-s mean magnetic field as the background field, from which the magnetic field data were converted into field-aligned coordinates. The fast Fourier transform technique was performed on 4,096 data points with an input step length of 512 points. Wave power was calculated utilizing the method described by Allen et al. (2015). Daily plots of Electric and Magnetic Field Instrument Suite and Integrated Science data were generated, and EMIC wave events were identified visually. A total of 19 and 14 EMIC wave events were selected for VAP A and VAP B, respectively. For each wave event, the UT, ILat, MLT, and ellipticity values for the peak power density of the EMIC waves were documented. Each wave event needed to be observed for at least 1 min UT to avoid being classified as background noise. Events were also cataloged by wave band.

Figure 3 shows an example of an EMIC wave event detected by VAP A from 15:50 to 16:40 UT on 24 June 2015, during the recovery phase of the storm. Two EMIC waves (one H^+ band and one He^+ band) were observed during this period, split by the He^+ gyrofrequency. The lower band was centered around 16:10 UT, and the higher band was centered around 16:11 UT. The frequency at peak power of the lower band was 1.58 Hz, and that of the higher band was 3.03 Hz. The wave data at peak power for both bands are listed in Table 1. These two events were also observed by Swarm A and Swarm C at an altitude of 460 km at nearly the same UT and MLT. This will be addressed in more detail in section 4.3.

3. Observations

3.1. Solar Wind and Geomagnetic Conditions

This study used the OMNI data set with a resolution of 5 min. The data were time shifted to the bow shock. Figure 4 shows the y and z components of the interplanetary magnetic field (IMF B_y and IMF B_z), the dynamic pressure of the solar wind (P_{dyn}), the magnetic indices *AE* (auroral electrojet) and *SYM-H*, and the merging electric field (E_m; Newell et al., 2007) during the geomagnetic storm from 21 to 29 June 2015. The storm began on 21 June after IMF B_z turned southward with a large number of oscillations (−30 to 30 nT). These fluctuations in IMF B_z coincide with a spike in P_{dyn} (47.2 nPa) observed at 19:45 UT on 22 June.

Table 1
Two-Band EMIC Waves Observed Coordinately by Swarm A in the F Region and by VAP A in the Magnetosphere, on 24 June 2015

Satellite	Date	UT (HH)	MLT (HH)	ILat (deg)	Frequency (Hz)	Maximum power (log (nT^2/Hz))	Normal angle (deg)	Ellipticity	L (R_E)
Swarm A	20150624	15:41	22:04	48.58	3.33	−3.47	0.67	−0.09	2.29
Swarm A	20150624	15:41	22:05	46.70	1.75	−2.64	0.58	−0.18	2.13
Swarm A	20150624	16:03	22:08	−48.13	2.59	−3.29	34.91	0.06	2.30
Swarm A	20150624	16:02	22:11	−43.51	1.44	−4.45	31.26	−0.03	1.93
VAP A	20150624	16:11	21:23	58.94	3.03	−2.72	22.35	0.03	3.76
VAP A	20150624	16:10	21:23	58.94	1.58	−0.03	4.22	−0.58	3.76

Note. The wave informations for the maximum power density of each wave event is shown. Dates are formatted as YY/MM/DD. EMIC = electromagnetic ion cyclotron; VAP = Van Allen Probe; UT = universal time; MLT = magnetic local time; ILat = invariant latitudes.

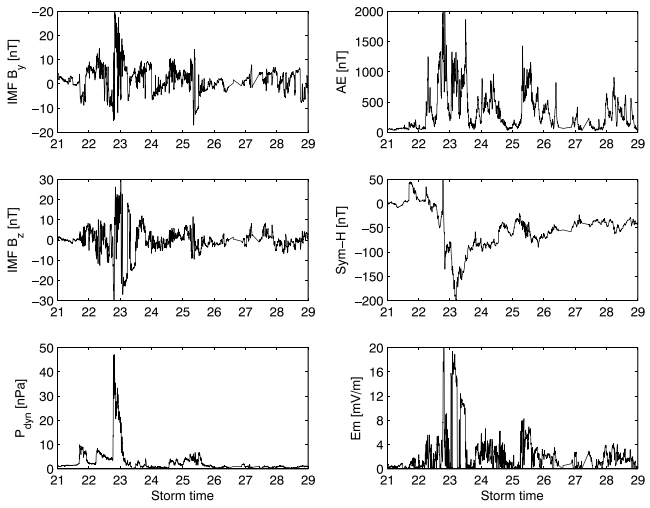

Figure 4. Temporal variations of the 5-min averaged solar wind and interplanetary magnetic field (IMF) data from 21–29 June 2015. The data have been time shifted to the bow shock. (left column, from top to bottom) IMF B_y, IMF B_z, and solar wind dynamic pressure (P_{dyn}). (right column, from top to bottom) magnetic indices, *AE* and *SYM-H*, as well as the merging electric field, $E_m = V^{4/3}(B_y^2 + B_z^2)^{1/3}\sin(\theta/2)^{8/3}$, where V is solar wind velocity, B_y and B_z are IMF components, θ is the clock angle, $\theta = \arctan(B_y/B_z)$ (Newell et al., 2007). We commonly divided the value by 3,000 in order to obtain it in millivolts per meter.

SYM-H is also observed to possess positive values during this period, indicating magnetospheric compression. Minimum *SYM-H* occurred at approximately 04:25 UT on 23 June with a value of −207 nT. Here we defined the main phase as the period from the event onset to the *SYM-H* minimum (start time to 04:25 UT), and the recovery phase follows the point of minimum *SYM-H* to the end of 29 June. The *AE* index showed that a series of substorms occurred during the storm period. The substorm at 09:30 UT on 24 June (peak *AE* index of 965 nT) was weaker than that at 07:40 UT on 25 June (peak *AE* index of 1,428 nT). Both these substorms occurred during the recovery phase. The merging electric field also exhibited several major peaks, which were almost synchronous with those of the *AE* index.

3.2. MLT and ILat Distributions of EMIC Waves

EMIC waves were observed on both the dayside and nightside, in subauroral regions by the Swarm satellites and in auroral regions by VAPs. The event numbers are listed in Table 2. For each Swarm and VAP satellite, EMIC wave occurrence rates were determined in an ILat vs. MLT format with each bin representing 2° ILat and 2-hr MLT. The occurrence rate was determined by taking the ratio of the total amount of EMIC wave observation time to the total dwell time in that respective bin. The local time and ILat distributions of the occurrence frequency of EMIC waves observed by the Swarm satellites and VAPs are shown in Figure 5. Regions in which the Swarm satellites (VAPs) had a dwell time of less than 30 min (1 hr) are not shown. Swarm events are shown separately for the Northern and Southern Hemispheres. The occurrence frequency of EMIC waves was highest in the 22:00–24:00 MLT sector (on the nightside), and the northern (summer) occurrence was higher than the southern (winter) occurrence. The occurrence rate was higher in the 00:00–02:00 MLT sector (on the nightside) than in the 12:00–14:00 MLT sectors (on the dayside) in the Northern Hemisphere but not in the Southern Hemisphere. The prenoon sector (10:00–12:00 MLT) shows higher occurrence rate than the afternoon sector (12:00–14:00 MLT). The local time distribution of the occurrence rate of storm time EMIC waves are different from those of statistical results by H. Kim et al. (2018) based on Swarm wave events from December 2013 to June 2017. In their work quite comparable occurrence distribution was found around the noon and midnight, while in the present work, we found maximum occurrence in the premidnight sector when compared to the prenoon, postnoon, and postmidnight sectors. The local time difference in the occurrence rates will be discussed in more detail in section 4.2.

For the VAP A events, in the dusk sector, the peak occurrence was observed in the 14:00–16:00 MLT sector around 60° ILat (4 R_E). The peak occurrence of VAP B events was observed in the 14:00–18:00 MLT sector around 60°–65° ILat (4–5.5 R_E). The occurrence probability was higher in the afternoon sector than in the premidnight sector. There was an overlap between the orbits of the Swarm satellites and VAPs in the

Table 2
The Event Numbers of EMIC Waves as Observed by Swarms and VAPs in the Daytime and Nighttime

Satellite	Day, NH	Night, NH	Day, SH	Night, SH
Swarm A	7	12	8	9
Swarm B	5	8	8	4
Swarm C	7	12	8	9
VAP A	10	9	—	—
VAP B	11	3	—	—

Note. VAPs events were detected near the magnetic equatorial regions, and the Northern and Southern Hemispheres were not differentiated. EMIC = electromagnetic ion cyclotron; VAP = Van Allen Probe; NH = Northern Hemisphere; SH = Southern Hemisphere.

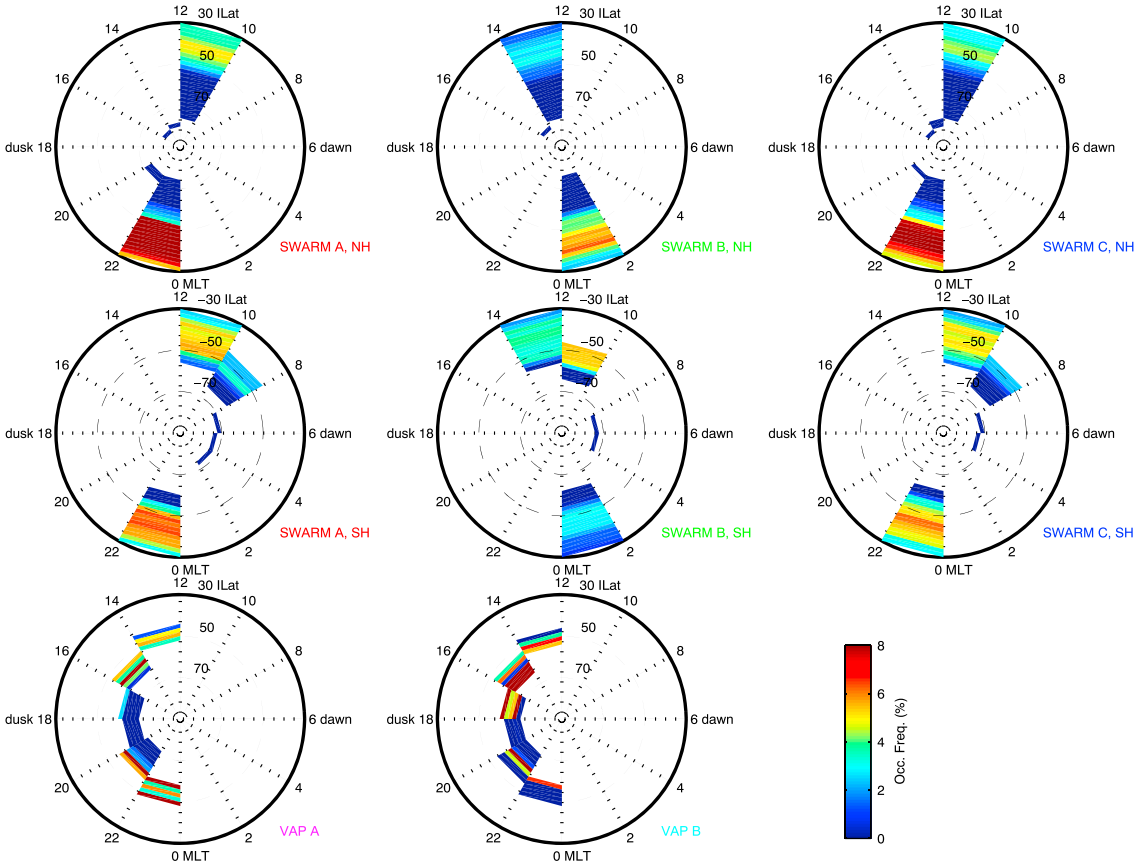

Figure 5. A plot of the occurrence frequency of EMIC waves as detected by Swarm and Van Allen Probes during the storm period in the same format as Figure 1. Over-plotted circles represent 30°, 50°, and 70° ILat, respectively. EMIC = electromagnetic ion cyclotron.

premidnight sector at almost the same time, which made coordinated observations of EMIC waves possible and these will be shown in section 4.3.

3.3. Temporal and Latitudinal Variations in EMIC Waves

The temporal and latitudinal variations in EMIC waves on both the dayside and the nightside in both hemispheres are shown in Figure 6. Also plotted are the values of the *SYM-H* index, which represent the storm phases during EMIC wave events. Superimposed onto Figure 6 is a simulated plasmapause location based on Moldwin et al. (2002), which estimates the location from measurements of *Kp*. It contained the standard deviations of the measured locations of the plasmapause in comparison with the locations determined by a linear best fit. The average positions of the plasmapause are indicated, with error bars, by a yellow line in the 12:00–18:00 (Figures 6a and 6c) and 18:00–24:00 MLT (Figures 6b and 6d) sectors. The variability in the location of the plasmapause for a given *Kp* value was attributed to the imperfect characterization of convection history achieved using a single *Kp* value (Moldwin et al., 2002). Part of the variability in the dusk sector was due to the small-scale surface features in the form of bulges and drainage features (Moldwin et al., 2002). The trajectories of the VAPs during which EMIC wave could be detected are marked by gray lines.

VAP events are represented by asterisks and Swarm events by dots. Here the storm time and ILat correspond to the location of the peak power density. On the dayside (14:00–18:00 MLT, Figures 6a and 6c), VAP events were observed during the main and recovery phases, with more events during the recovery phase. On the nightside (20:00–01:00 MLT, Figures 6b and 6d), VAP events occurred during the main phase and early recovery phase before 25 June. VAP events were absent within a period of ±1 hr when the *SYM-H* index was at a minimum around 04:23 UT on 23 June, although the VAPs were in regions where waves could be detected (VAP A flew from about 70° to 33° ILat and from around 20:00 to 03:00 MLT, and VAP B flew from about 70° to 62.8° ILat and from around 19:00 to 21:00 MLT within 03:25–05:25 UT on 23 June).

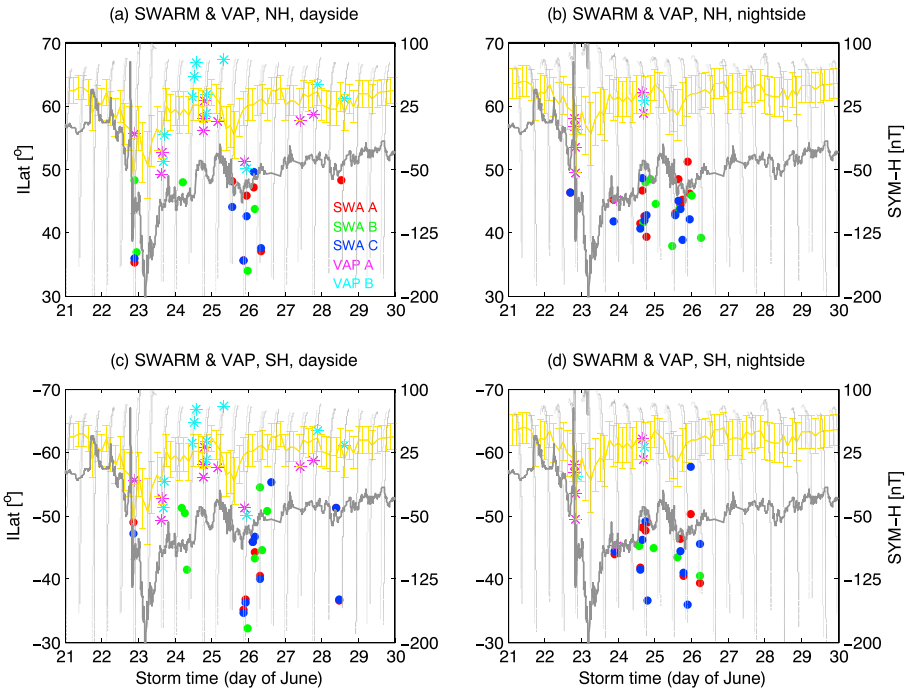

Figure 6. The variation of EMIC waves detected by VAPs A and B and by Swarms A, B, and C as a function of invariant latitude and storm time (days of June). *SYM-H* evolution is superimposed. An average plasmapause location as described by Moldwin et al. (2002) in the 12:00–18:00 and 18:00–24:00 MLT sector is over-plotted with error bars. The VAP A and B orbits when they are able to detect EMIC waves are shown in light and dark gray lines, respectively. The top panels (a, b) are in the NH; bottom (c, d) are in the SH. Left panels (a, c) are on the dayside; right (b, d) are on the nightside. VAP A events are marked in magenta, VAP B in light blue, Swarm A in red, Swarm B in green, and Swarm C in blue. EMIC = electromagnetic ion cyclotron; VAP = Van Allen Probe; MLT = magnetic local time; NH = Northern Hemisphere; SH = Southern Hemisphere.

The ILats of VAP events tend to shift equatorward as *SYM-H* decreases and poleward as *SYM-H* increases, which is consistent with the erosion of the plasmasphere during the main phase of storms and its expansion during the recovery phase, as indicated by the modeled plasmapause (Moldwin et al., 2002). With an increase in geomagnetic activity, both the location of the maximum energy density of the ring current and plasmapause tend to move to lower L shells. Thus, waves tend to occur at lower latitudes. This indicates that the cold and dense plasma in the plasmasphere or plume is important for the generation of EMIC waves, which is consistent with the result of Lee et al. (2008). Lee et al. (2008) solved the coupled plasma wave equation by adopting the invariant imbedding method. They showed that Pc1–2 waves were strongly associated with the presence of various ions in the magnetosphere. They suggested that the composition of heavy ions could be monitored by checking the peak frequencies of waves. Furthermore, Magnetospheric compressions can impact the locations of EMIC wave source regions. Here such compression was observed around 19:45 UT on 22 June.

During the expansion phase on 22 June, Swarms observed EMIC waves in the prenoon and postnoon sectors around 20:00–21:00 UT (Figures 6a and 6c). VAP A detected EMIC waves around 21:00 UT at higher ILats (55.6° ILat) in the late-afternoon sector (Figures 6a and 6c). These EMIC waves might be related to the sudden increase in the dynamic pressure that began at 19:45 UT on 22 June 2015 (see Figure 4).

More Swarm events occurred during the recovery phase as compared to those during the main phase. During the recovery phase, the nighttime wave events (Figures 6b and 6d) detected by Swarm A and Swarm C occurred about 2 days earlier than on the dayside (Figures 6a and 6c). The daytime events were detected on 26 June, whereas the nighttime events occurred on 24–25 June and around 26 June. This daytime-nighttime asymmetry existed in both hemispheres. In addition, the postnoon events (Swarm B) tended to occur earlier than the prenoon events (Swarms A and Swarm C, Figures 6a and 6c). In both hemispheres, Swarm B observed EMIC waves on 24 June, whereas Swarms A and Swarm C detected the events on 25 June. On the nightside (Figures 6b and 6d), the premidnight events (Swarms A and Swarm C) occurred earlier than

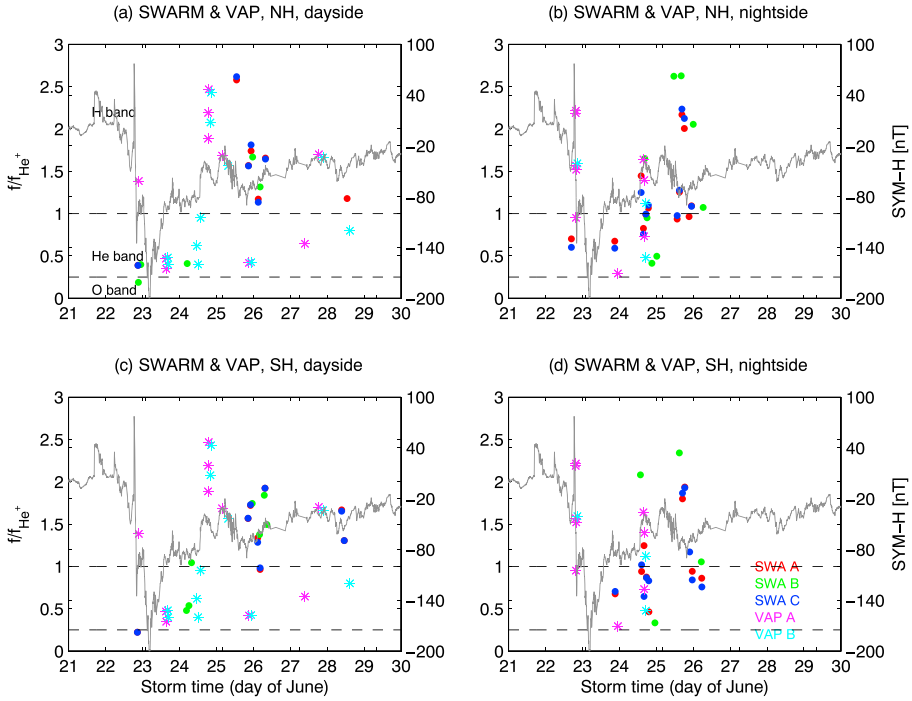

Figure 7. Scatterplot of normalized frequencies of EMIC waves versus storm time. *SYM-H* evolution is superimposed. The top panels (a, b) are in the NH; bottom (c, d) are in the SH. Left panels (a, c) are on the dayside; right (b, d) are on the nightside. VAP A events are marked in magenta, VAP B in light blue, Swarm A in red, Swarm B in green, and Swarm C in blue. The equatorial He^+ (normalized frequency = 1), and the O^+ gyrofrequencies (normalized frequency < 1/4) are indicated by dashed lines. Different band ranges are indicated in the left upper figure panel.
EMIC = electromagnetic ion cyclotron; NH = Northern Hemisphere; SH = Southern Hemisphere; VAP = Van Allen Probe.

the postmidnight events (Swarm B). These differences in response times will be examined in more detail in section 4.2.

3.4. Wave Bands

Figure 7 presents the temporal variations in the normalized frequency (normalized to the equatorial He^+ gyrofrequency) on both the dayside and the nightside in the Northern and Southern Hemispheres. The dashed lines indicate the gyrofrequencies of He^+ (normalized frequency = 1.0) and O^+ (normalized frequency < 0.25). The wave events have been mapped along the magnetic field lines to the equatorial region, where the gyrofrequencies of He^+ and O^+ were calculated, using the Tsyganenko 1996 model (Tsyganenko, 1995; 1996). O^+ band EMIC waves were observed during the main phase by Swarm B in the postnoon sector (~13:00 MLT, Figures 7a and 7c) in the Northern Hemisphere, while Swarm A and Swarm C observed O^+ band waves in the prenoon sector (~10:30 MLT) in the Southern Hemisphere. These observations are consistent with peak occurrence region of O^+ band EMIC waves (Saikin et al., 2015; Yu et al., 2015). By utilizing data from VAP A alone, Yu et al. (2015) revealed that most O^+ band events were observed between 06:00 and 13:00 MLT. Following their work, Saikin et al. (2015) made an extension on these results by incorporating data from both VAPs and found that O^+ band EMIC waves displayed one peak region in the morning sector in lower L shells ($L < 4R_E$).

During the recovery phase from 23 to 25 June, most of the Swarm and VAP events were He^+ waves (0.25 < normalized frequency < 1.0). During the later recovery phase, after 25 June, most of the Swarm wave events corresponded to the H^+ band (normalized frequency of between 1 and 4), except in the Southern Hemisphere nightside. Both ionospheric wave frequency and power are higher in the summer hemisphere than in the winter hemisphere. The hemispheric differences in wave frequency and power density will be revisited in section 4.2. In the case of the VAP events during the recovery phase after 25 June, H^+ and He^+ waves coexisted. Most of the Swarm event waves were linearly polarized. This is consistent with previous results

for low altitudes, according to which waves observed by the Challenging Minisatellite Payload satellite had features dominated by linear polarization(e.g., Park et al., 2013) .

4. Discussion

4.1. Controlling Factors

The relationship between the dynamic pressure and increased EMIC wave activity has been demonstrated in the literature (Anderson, 1993). During compression events (i.e., high P_{dyn}), the magnetic field strength undergoes large relative changes around noon in the higher L shells, and the proton anisotropy can increase as a result of either Shabansky orbits (McCollough et al., 2009; Shabansky, 1971) or perpendicular adiabatic ion heating (Anderson, 1993). Anderson (1993) reported a strong correlation between magnetospheric compressions and EMIC wave observed in space. They found that in the 08:00–16:00 MLT sector, 47% of sudden increases in the magnetic field strength were associated with EMIC waves. Engebretson et al. (2002) found that EMIC waves were preferably associated with significant compressions of the magnetosphere according to polar observations. When the magnetosphere is compressed by large changes in the dynamic pressure of the solar wind associated with the sudden commencement of a storm, anisotropic ion distributions can be generated in the magnetosphere, which makes the plasma in a given flux tube more unstable (Engebretson et al., 2002). Therefore, the plasma environment in the dayside outer magnetosphere becomes more favorable for the generation of EMIC waves (Allen et al., 2016; McCollough et al., 2010). McCollough et al. (2009) outlined several mechanisms for the temperature anisotropy of warm plasma during the magnetospheric compression. The first was related to the drift shell splitting, which occurred in any field that has been distorted by the solar wind. With significant distortion, local regions of minimum B values could be produced away from the magnetic equator in the dayside magnetosphere (McCollough et al., 2009; McCollough et al., 2010; McCollough et al., 2012; Shabansky, 1971). Particle executing Shabansky orbits could lead to anisotropies at the equator. These were favorable locations for the generation of EMIC waves (Allen et al., 2013, 2015, 2016; Liu et al., 2012, 2013).

Another mechanism was related to adiabatic energization, which occurred when magnetospheric compression happened sufficiently slowly that all adiabatic invariants were conserved, but the strengthening field increased the perpendicular energy (McCollough et al., 2009). In accordance with this paradigm, both VAPs and Swarm satellites observed EMIC waves when the solar wind pressure suddenly increased to 47.2 nPa and the *SYM-H* quickly changed to positive values during the main phase of the storm. Engebretson et al. (2015) presented the VAP observations of the pressure effects on 23 February 2014, when H^+ waves extended over 8 hr from the late morning sector to the dusk sector. In the present study, VAPs observed H^+ band waves whereas Swarm satellites observed He^+ and O^+ band waves on the dayside. We also note that there were two increases in the dynamic pressure (about 10 nPa) on 21 and 22 June, when no EMIC waves were observed by either VAPs or Swarm satellites. Park et al. (2013) could find no evidence that the dynamic pressure controlled the rate of occurrence of Pc1 waves at low Earth orbit. There might be a critical threshold value for the increase in the dynamic pressure required to generate EMIC waves in the inner magnetosphere.

During the expansion phase, waves were also observed by VAPs and Swarm satellites in the premidnight (around 22:00–24:00 MLT) sector, except for the southern ionosphere. A previous work suggested that the dynamic pressure mainly affected dayside waves (Anderson, 1993). The waves in the premidnight sector might be related to the substorm processes (Engebretson et al., 2015; Keika et al., 2013; see the values of the *AE* index in Figure 4).

The lack of observations of waves by the VAPs around the *SYM-H* minimum might be due to the suppression of waves by the abundance of O^+ ions in accordance with previous results (McCollough et al., 2009; Thorne & Horne, 1997). Using simulations, Thorne and Horne (1997) demonstrated that an increase in the fraction of O^+ ions in the ring current during storms could affect the excitation of EMIC waves. During intense storms, when the concentration of O^+ ions was $\geq$ 60%, cyclotron absorption by resonant O^+ could become so severe that it totally suppressed the wave excitation in the band above the gyrofrequency of O^+. Furthermore, when examining EMIC wave excitation through compression related growth, McCollough et al. (2009) found that an increase in the abundance of warm oxygen suppressed wave growth, which supported the result of Thorne and Horne (1997). Similarly, ground-based observations failed to observe EMIC waves during the main phase of storms (Engebretson, Lessard, et al., 2008; Engebretson, Posch, et al., 2008), which they attributed to the ionospheric screening effects or unfavorable locations of ground stations. Our observations

are consistent with their observations. In the present work, we provide evidence that EMIC waves in both the magnetosphere and the ionosphere were absent around the *SYM-H* minimum (Swarm A, Swarm C, and Swarm B observed EMIC waves before 21:00 UT on 22 June, not around the *SYM-H* minimum).

During the recovery phase of the storm, VAPs observed relatively high occurrence rates of waves in the afternoon sector that corresponded to H^+ and He^+ band events, consistent with previous results (Meredith et al., 2014; Saikin et al., 2015). This can be explained by the coexistence of cold dense plasma and hot anisotropic ions from the expanding/contracting plasmasphere or plasmaspheric plumes and the ring current, respectively. Allen et al. (2016) studied the plasma conditions associated with EMIC waves during 10 years of observations by the Cluster satellites and found that an overlap between a cold plasmaspheric plume and the ring current in the afternoon sector was a favorable condition for the occurrence of waves. As an example, Figure 8 shows EMIC wave events and the corresponding spectra of H^+, He^+, and O^+ recovered by the Helium, Oxygen, Proton, and Electron Mass Spectrometer, as well as the electron density measured by the VAP Electric Fields and Waves instrument between 15:00 and 16:00 UT in the afternoon sector on 23 June. The black vertical dashed line in the bottom panel indicates the location of the plasmapause identified by adopting the method used in Heilig and Lühr (2018), that is, a factor of 5 drop or more over an L range of less than 0.25 R_E. This gradient threshold (Heilig & Lühr, 2018) is about twice as large as those applied by previous studies (He et al., 2017). The first EMIC wave was generated close to the plasmapause but slightly outside, where low- and high-energy ions coexisted, which indicated that the EMIC wave was generated when the ring current and plasmasphere or plasma plume particles overlapped. The second EMIC wave occurred outside of the plasmapause. We checked the other VAP wave events in the afternoon sector during recovery phase and found that 11 events occurred within or close to the plasmapause where low- and high-energy ions coexisted (Electric Fields and Waves data were unavailable for five events, and four events occurred outside of the plasmapause). Previous work have suggested that the plasmapause and plasmaspheric plumes are favorable locations for the occurrence of EMIC waves (e.g., Fraser & Nguyen, 2001; Horne & Thorne, 1993; Usanova et al., 2013). Usanova et al. (2013) reported that EMIC waves were about 20 times more likely to be observed inside a plasmaspheric plume than outside of such a plume. Fraser and Nguyen (2001) found that the afternoon EMIC waves occurred in the plasma bulge region, where H^+ ions in the ring current and dense cold plasma overlapped. Fraser et al. (2010) suggested during geomagnetic storms, the ring current hot ions were injected into populations of cold heavy ions in the inner magnetosphere. Blum et al. (2009) disclosed a difference according to local time in the occurrence frequency of EMIC waves in the magnetosphere. They found that the area of the greatest concentration of enhanced EMIC waves extended from noon to dusk. They suggested that although the temperature anisotropy caused elevated occurrences from dusk to dawn (e.g., Allen et al., 2016; Min et al., 2012), the instability threshold for the generation of waves was more easily attained from noon to dusk due to the presence of more cold plasma.

During the late recovery phase, large numbers of Swarm H^+ band EMIC waves occurred in the prenoon and premidnight sectors, except for the nighttime winter (i.e., the Southern Hemisphere). Few studies have focused on the wave band observed below 2 R_E except that of Kasahara et al. (1992). They found that in the lower L shells (1.5 R_E), H^+ band waves were more prominent than He^+ band waves. Our observations are consistent with these findings. Kasahara et al. (1992) found that the peak occurrence of waves took place in the evening sector (16:00–20:00 MLT) in the low-L shell region. Our study also disclosed that the occurrence frequency of waves was higher in the nighttime than in the daytime in the ionosphere. We associate these waves during the recovery phase of the storm with the occurrence of substorms. Bossen et al. (1976) reported that almost every EMIC wave observed by the ATS-1 satellite was associated with a substorm. As mentioned in section 3.1, there were two substorms, which occurred on 24 and 25 June (see the values of the *AE* index in Figure 4). Substorm-related injections of anisotropic energetic ions in the ring current aided in the generation of waves. These high-energy ions can drift westward to the dusk and noon sectors because of the magnetic field gradient and curvature forces. This would explain why the first observations of waves were made in the premidnight sector by Swarm A and Swarm C, followed by the postnoon sector by Swarm B, and finally the prenoon sector by Swarm A and Swarm C. The substorm on 24 June was weaker than that on 25 June. During the weaker substorm, the energetic ions might not have been able to generate waves in the noon sector. This might explain the lack of waves in the noon sector on 24 June, although there were waves in the premidnight sector. Thus, it can be concluded that the auroral activity (reflected in the *AE* index) might affect the occurrence of EMIC waves on the nightside during the storm recovery phase of

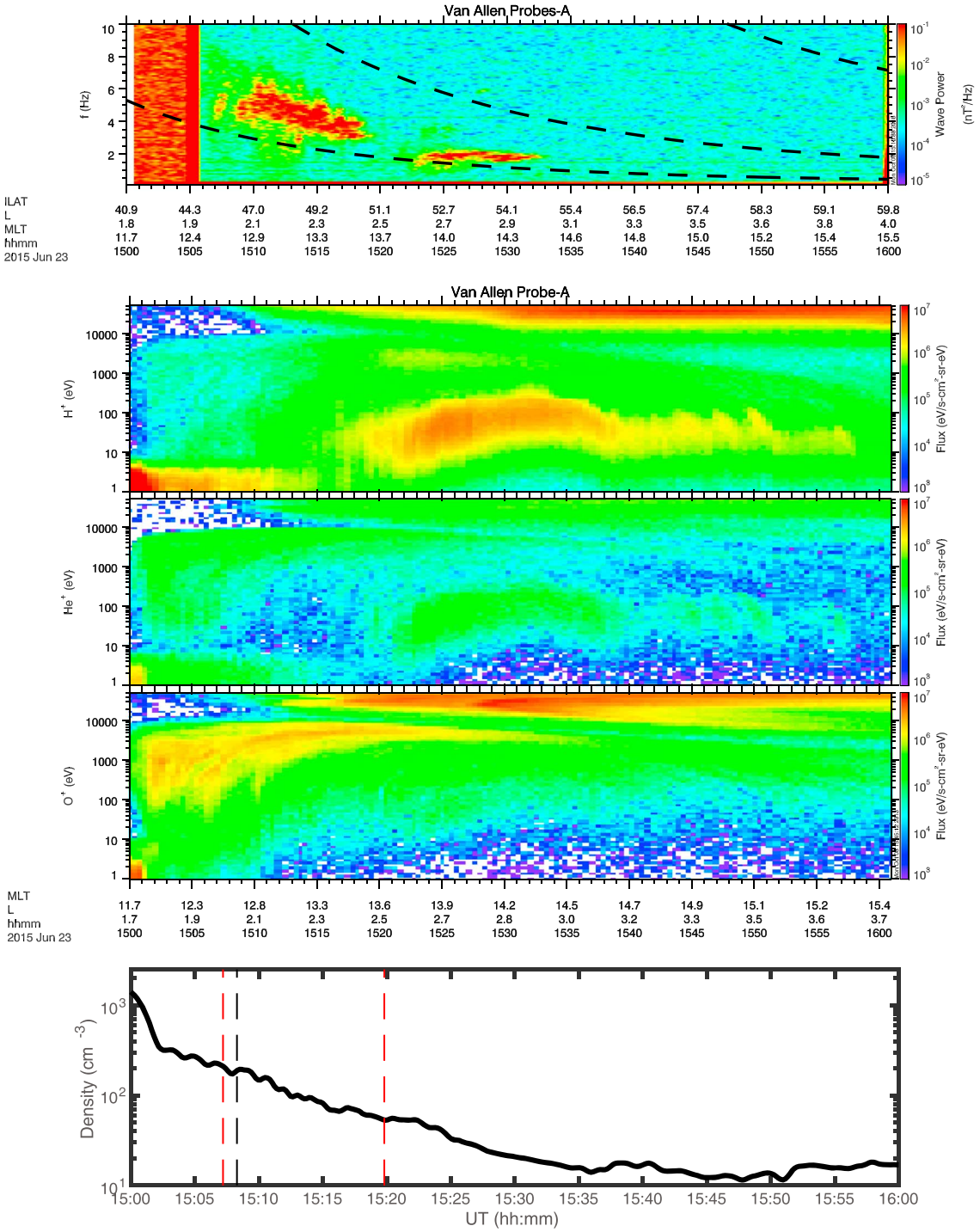

Figure 8. (top panel) The wave spectrogram as a function of frequency and universal time. MLT, L shell value, and ILat are given together with the UT. (middle panel) The spectrum of H^+, He^+, and O^+ ions for ion energy from 1 eV to 50 keV. MLT and *L* are given together with UT. (bottom panel) The electron density measured by VAP Electric Fields and Waves instrument. Red vertical dashed lines represent the EMIC wave period. Black dashed line denotes the plasmapause location by adopting the same method of Heilig and Lühr (2018). MLT = magnetic local time; ILat = invariant latitude; UT = universal time; VAP = Van Allen Probe; EMIC = electromagnetic ion cyclotron.

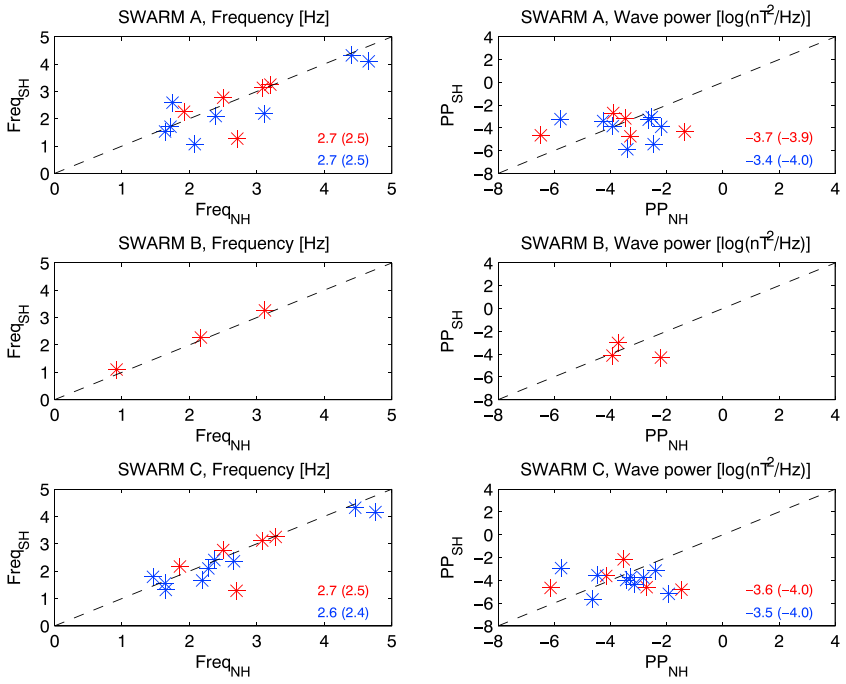

Figure 9. Comparison of EMIC wave frequency (left column) and power (right column) from the Northern (local summer) and Southern (local winter) Hemispheres for Swarms A, B, and C from the descending or ascending orbits. Dayside data are red asterisks; nightside data are blue asterisks. The dashed line is the 1:1 line. The average frequency and power are given. The values out of the brackets are in the Northern (summer) Hemisphere, and those in the brackets are in the Southern (winter) Hemisphere. EMIC = electromagnetic ion cyclotron; NH = Northern Hemisphere; SH = Southern Hemisphere.

storms. The strength of the *AE* might affect the occurrence of waves on the dayside. Future work will use an ion drift model to test this speculation in more detail.

4.2. Hemispheric and Local Time Differences

There were differences in the frequencies and power densities of ionospheric EMIC waves in the Northern and Southern Hemispheres. In Figure 9 the frequency (left column) and power density (right column) of waves in both hemispheres are shown separately for Swarm A, Swarm B, and Swarm C. These events were observed during the same descending or ascending orbit in the same MLT sector, with UT differences of less than 25 min, and 83% of differences in L values were less than 0.5 R_E. The data points represented orbits in which Swarm observed EMIC wave packets in both hemispheres and as such assumed that they were from the same source region. Daytime (nighttime) observations are shown in red (blue). The average frequency and wave power are given for Swarm A and Swarm C events. A Wilcoxon rank-sum test was employed to test for statistical significance (Wild & Seber, 2000). The probabilities with nonequal means were 100% and 57% on the dayside and nightside for Swarm A frequency, 100% and 67% for Swarm C frequency, 84% and 34% for Swarm A wave power, and 55% and 31% for Swarm C wave power, respectively. The statistical significances of the nonequal means were fairly well. The mean wave frequency and power density were both higher in the Northern (summer) Hemisphere than in the Southern (winter) Hemisphere. Alternatively, we have calculated the average frequency and power density of all wave events in the two hemispheres and the conclusions remained the same. This might indicate that the ionospheric electron density affected the propagation of waves from the magnetosphere to the ionosphere. This process might be related to the Alfvén wave speed, $V_A = \sqrt{B^2/m_i n\mu_0}$, where B is the magnetic field strength, m_i is the ion mass, n is the electron density, and μ_0 is the magnetic permeability. V_A is inversely proportional to the ionospheric electron density. A higher electron density in the ionospheric F region can reduce the Alfvén wave speed to a greater extent and thus confine the wave power to the F region. A Lower electron density in the F region might cause more leakage of waves to the ionospheric E region or the ground. The hemispheric differences in wave frequency might arise because magnetospheric wave packets could be distorted in the dispersive ionosphere. Because the difference in electron density between the Northern (summer) and Southern (winter) Hemispheres, the

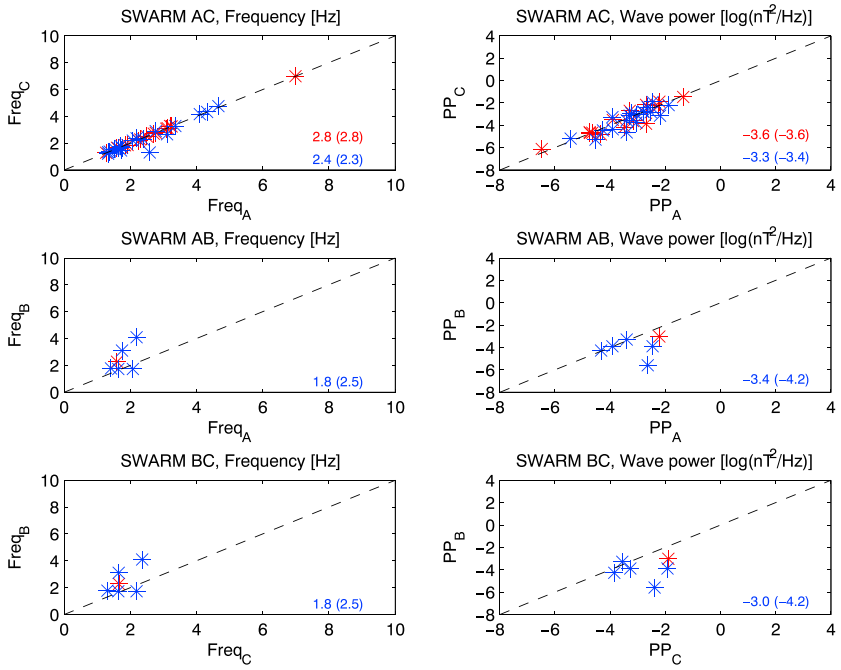

Figure 10. Comparison of EMIC wave frequency (left column) and wave power (right column) observed almost simultaneously by Swarm A versus B, Swarm A versus C, and Swarm B versus C. Both hemispheres are shown together. Dayside data are red asterisks; nightside data are blue asterisks. The dashed line is the 1:1 line. The average frequency and power are given. The values out of the brackets are for the *x* axis parameter, and those in the brackets are for the *y* axis parameter. EMIC = electromagnetic ion cyclotron.

extent of distortion of the wave signal could be different in the two hemispheres. This might result in a difference in the frequency that corresponds to the maximum power density in the two hemispheres.

The Swarm A and Swarm C satellites and Swarm B satellite traversed the wave regions almost simultaneously but were separated by an MLT interval of about 2 hr. This provided us with an opportunity to compare the differences in wave frequency and power density according to MLT during storm periods. For the selection of events observed by two satellites, the difference in UT was less than 50 min, the difference in MLT was less than 3 hr, and the difference in ILat was less than 9° (the difference in L shell was less than 0.6 R_E). In Figure 10, the left column shows a comparison of Swarm frequency values and the right column shows a comparison of Swarm power density values in both hemispheres. Again, dayside (nightside) observations are shown in red (blue). From top to bottom, the comparisons are: Swarm A versus Swarm C, Swarm A versus Swarm B, and Swarm B versus Swarm C. The average frequency and wave power are given. The values in brackets are the *y* axis parameters, and those outside of brackets are the *x* axis parameters. In general, Swarm A and Swarm C measured similar frequencies and power densities because they flew side by side with a longitudinal separation of only 1.4°. However, Swarm A and Swarm C generally observed lower frequencies and higher power densities than Swarm B. This indicates an obvious difference according to local time in EMIC waves observed in the ionosphere in response to geomagnetic storms. The difference according to local time in the wave frequency and power density in the ionosphere during storm periods has not been addressed in the literature.

4.3. Combined Observations

At approximately 16:00 UT on 24 June, VAP A, together with Swarm A and Swarm C, detected a two-band wave event in the 21:00–22:00 MLT sector. The wave information from VAP A and Swarms A is listed in Table 1. The differences in MLT, ILAT, and L shells between VAP and Swarm were 30–40 min, 10–15°, 1.5–1.8 R_E, respectively. Figure 11 (top panel) shows a schematic summary of the locations on the polar map (ILat versus MLT coordinate system) where EMIC waves were detected around 16:00 UT. The VAP footprints are shown from 15:00 UT to 17:00 UT. The Swarm A and Swarm C traces (red and blue lines) extended from 15:30 to 15:45 UT in the Northern and from 15:56 to 16:10 UT in the Southern Hemisphere. The Swarm B trace (green line) extended from 15:59 to 16:15 UT in the Northern Hemisphere, and from 15:30 to 15:45

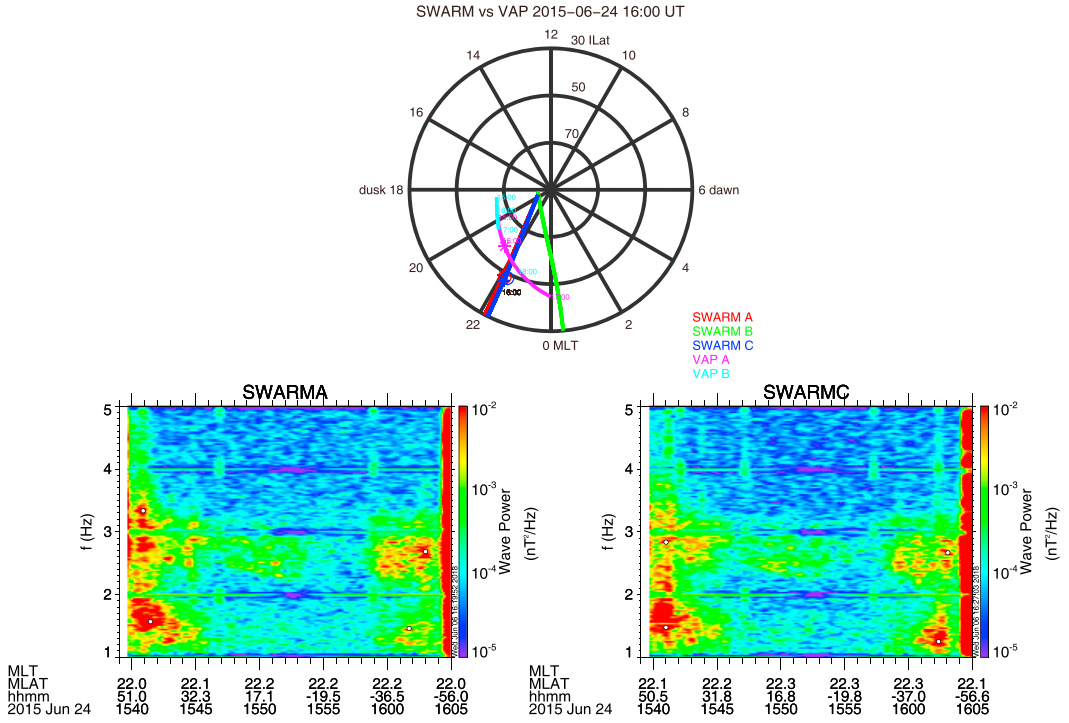

Figure 11. (top panel) Plot of the MLT (magnetic local time) versus ILat (magnetic latitude) locations of VAP A (magenta) and B (light blue), Swarm A (red), Swarm B (green), and Swarm C (blue). Over-plotted circles represent 30°, 50°, and 70° ILat, respectively. The ionospheric footprint of VAP is shown as a function of time from 15:00 to 17:00 UT. The start and stop time of Swarm B trace is from 15:59 to 16:15 UT in the Northern Hemisphere and from 15:30 to 15:45 UT in the Southern Hemisphere. The VAP EMIC wave is indicated by an asterisk, and Swarm waves in the Northern Hemisphere are indicated by circles and in the Southern Hemisphere by asterisks. (bottom two panels) Wave spectrograms of the magnetic fields measured by Swarms A and C at approximately 16:00 UT on 24 June 2015. Two-frequency band EMIC waves can be identified at subauroral latitudes in the 22:00 MLT sector. VAP = Van Allen Probe; EMIC = electromagnetic ion cyclotron.

UT in the Southern Hemisphere. The location of the EMIC wave observed by VAP A is indicated by the magenta asterisk. The Swarm A waves in the northern midlatitudes are indicated by circles, and those in the southern midlatitudes are indicated by asterisks. At approximately 16:00 UT, VAP A was located near 22:00 MLT, while VAP B was located near 20:00 MLT and did not detect the event at that local time. This indicates that the wave region extended over an MLT interval of less than 2 hr in the westward direction. The two-band wave event observed by VAP A is illustrated in Figure 3. The wave spectrograms from the observations by Swarm A and Swarm C in the premidnight sector (22:00 MLT) are shown in the bottom two panels of Figure 11. Swarm B did not detect this event in the postmidnight sector (01:00 MLT: figure not shown). This indicates that the wave extended over an MLT interval of less than 5 hr in MLT. In their subsequent orbits, about 93 min later, Swarm A and Swarm C did not detect a similar wave. Hence, the wave duration of the wave was less than 186 min. Waves occurred in both Northern and Southern Hemispheres, which implied that the propagation of the waves from the magnetosphere was bidirectional.

The high-frequency band was centered at approximately 3.33 Hz in the Northern Hemisphere and 2.59 Hz in the Southern Hemisphere, whereas the low-frequency band was centered at approximately 1.75 and 1.44 Hz in the respective hemisphere (as indicated by the white circles in the Figure 3). These frequencies correspond to the maximum power density. The gyrofrequency of He^+ in the equatorial region was 2.12 Hz. Hence, the high-frequency wave was a H^+ wave, whereas the low-frequency wave was a He^+ wave. VAP A observed two wave bands, of which one had a frequency of 3.03 Hz and the other had a frequency of 1.58 Hz, both of which were comparable to those observed in the ionosphere. In the magnetosphere, the low-frequency band had a greater power value than the high-frequency band. This was similar to observations in the ionosphere, with the exception of values from Swarm A in the Southern Hemisphere. This might indicate that the same source caused the events in both the magnetosphere and the ionosphere. The source regions of such waves might

be located very close to the site of VAP A site near the equatorial plane (about 0.51° magnetic latitude) and in the inner magnetosphere (where $L = 3.76R_E$). The magnetospheric wave propagated along the northward and southward field lines into the ionosphere. Allen et al. (2013) found that the propagation of EMIC waves was bidirectional near their source regions and unidirectional when away from these regions. Liu et al. (2012) showed a prolonged EMIC wave event propagated in both directions in the outer magnetosphere ($L = 13R_E$). They provided the first direct evidence that the off-equatorial regions where the magnetic field reaches a minimum may be important regions for the excitation of waves.

The newly generated EMIC waves were often transverse and exhibited left-handed polarization, which was consistent with the direction of gyration of ions in the magnetic field. However, the lower-frequency wave in the magnetosphere displayed left-handed polarization, whereas the higher-frequency wave was linearly polarized. Previous researchers have proposed possible explanations for the observed linear polarization, characteristics of the wave in the VAP event (Saikin et al., 2015). The waves may have propagated toward the inner magnetosphere from a source region in a higher L shell. Linear polarization would thus only be an effect of wave propagation. Linear-mode EMIC waves have also been reported by missions other than the VAPs (Allen et al., 2015; Anderson et al., 1992; Min et al., 2012; X. Y. Wang et al., 2017). Denton et al. (1992) found that EMIC waves generated with linear polarization were more favorable for the obliquely propagating mode by using model efforts. Previous theoretical research has shown that a wave can change its polarization during its propagation to the ionosphere because of the abundance of heavy ions (He^+ and O^+; Johnson & Cheng, 1999; E.-H. Kim & Johnson, 2016; Young et al., 1981). Johnson and Cheng (1999) theoretically demonstrated how H^+ mode EMIC wave generated in the equatorial magnetosphere could propagate to the ground. They found that the strong coupling between the left hand and right hand polarized waves occurred near the He^+ and O^+ resonance locations, which allowed the equatorial H^+ mode waves to penetrate to the ionospheric altitudes. By using a recently developed 2-D full-wave code, K.-H. Kim et al. (2016) found that mode coupling from guided left hand polarized EMIC waves to unguided right hand polarized or left hand polarized waves (i.e., fast mode) occurred in the He^+-H^+ plasma. This enabled the waves to propagate to the ionosphere.

We have considered the issues known for Fourier analysis methods (Anderson et al., 1996; Denton et al., 1996; Lee & Angelopoulos, 2014). Should the spacecraft be observing multiple overlapping EMIC wave packets, this can throw off the polarization techniques being used. Anderson et al. (1996) found that the spectral analysis might underestimate the normal angle by 45° or more, due to the fluctuations in the polarization ellipse azimuth orientation. The constituent wave ellipticity values might be a median of superposed wave ellipticities (Denton et al., 1996).

The ionospheric ducting effect was not investigated in the present study (please refer to a comprehensive review by Lysak & Yoshikawa, 2013), because the signals of EMIC waves in the auroral regions were contaminated by field-aligned currents. To address the ionospheric ducting features of this event in more detail, data from ground-based coordinated observations must be included, which will be left for future work. The propagation Pc1–2 waves in the high-latitude ionospheric waveguide (duct) was comprehensively investigated by H. Kim et al. (2011) using ground-based magnetometer data obtained in Antarctica from −62° to −87° magnetic latitude. They found that poleward propagation was most efficient and that the wave power attenuation increased with an increase in wave frequency.

5. Conclusions

In this study, we have used high-resolution magnetic field data from the VAPs and Swarm constellation for the time periods of the 21–29 June 2015 magnetic storm. We have examined the temporal and spatial variations in EMIC waves, which were categorized into three bands. Hemispheric and local time variations were discovered. One wave event that was observed simultaneously by both VAPs and Swarm satellites was investigated. The results are summarized as follows:

1. The magnetospheric (VAP) EMIC waves had a maximum occurrence frequency in the afternoon sector in higher L shells, which was consistent with the results of previous statistical analysis. The ILat of the waves tended to shift equatorward during the expansion phase and poleward during the recovery phase, which was consistent with the movement of the plasmapause.

2. The ionospheric (Swarm) waves were observed in subauroral regions and occurred more frequently in the nighttime than in the daytime. They also exhibited less obvious movement in terms of variations in ILat, thus, less L shell dependence.
3. During the expansion phase, EMIC waves occurred on the dayside and in both the ionosphere and the magnetosphere in response to the dramatic increase in the dynamic pressure of the solar wind.
4. Waves were not observed in either the magnetosphere or in the ionosphere within ±1 hr when *SYM-H* index approached a minimum. This might have been the result of a suppression effect caused by an increase in the fraction of O^+ ions. During the early recovery phase, He^+ band EMIC waves were observed in the ionosphere and magnetosphere.
5. During the late recovery phase, H^+ band ionospheric EMIC waves were generated in response to substorms in the premidnight sector. The occurrence frequency of ionospheric EMIC waves in the noon sector was a function of the intensity of the substorm activity.
6. There were MLT and hemispheric differences in ionospheric wave frequency and power. Both frequency and power were higher in the summer hemisphere than in the winter hemisphere, which suggested that the ionospheric plasma density had an effect on the propagation of waves from the magnetosphere to the ionosphere. The wave frequency was lower and the power was higher in the premidngiht sector than in the postmidnight sector.
7. Coordinated observations of a two-band EMIC wave were reported from both Swarm A and VAP A in the premidnight sector, which indicated a common source of wave generation in the magnetosphere. The wave event was found to extend over an MLT of less than 5 hr and had a duration of less than 186 min in the ionosphere.

Our future work will investigate more storm events to confirm these newly identified features.

Acknowledgments
We thank the reviewers for their careful and helpful comments. The Swarm 50-Hz high-resolution magnetic field data were obtained from ftp://swarm-diss.eo.esa.int. The Van Allen Probe data were from the EMFISIS data directory at http://emfisis.physics.uiowa.edu. The solar wind and interplanetary magnetic field data were from NASA/GSFC'S Space Physics Data Facility's OMNIWeb at https://omniweb.gsfc.nasa.gov. The authors greatly appreciate the availability of data from these websites. This work is supported by the National Nature Science Foundation of China National Natural Science Foundation of China (41431073, 41674153, and 41521063). We would like to thank J. C. Zhang for fruitful discussion during the preparation of this manuscript.

References

Allen, R. C., Zhang, J. C., Kistler, L. M., Spence, H. E., Lin, R. L., Dunlop, M. W., & André, M. (2013). Multiple bidirectional EMIC waves observed by Cluster at middle magnetic latitudes in the dayside magnetosphere. *Journal of Geophysical Research: Space Physics*, *118*, 6266–6278. https://doi.org/10.1002/jgra.50600

Allen, R. C., Zhang, J. C., Kistler, L. M., Spence, H. E., Lin, R. L., Klecker, B., & Jordanova, V. K. (2015). A statistical study of EMIC waves observed by Cluster: 1. Wave properties. *Journal of Geophysical Research: Space Physics*, *120*, 5574–5592. https://doi.org/10.1002/2015JA021333

Allen, R. C., Zhang, J. C., Kistler, L. M., Spence, H. E., Lin, R. L., Klecker, B., & Jordanova, V. K. (2016). A statistical study of EMIC waves observed by Cluster: 2. Associated plasma conditions. *Journal of Geophysical Research: Space Physics*, *121*, 6458–6479. https://doi.org/10.1002/2016JA022541

Anderson, B. J. (1993). Electromagnetic ion cyclotron waves stimulated by modest magnetospheric compressions. *Journal of Geophysical Research*, *98*, 11,369–11,382. https://doi.org/10.1029/93JA00605

Anderson, B. J., Denton, R. E., & Fuselier, S. A. (1996). On determining polarization characteristics of ion cyclotron wave magnetic field fluctuations. *Journal of Geophysical Research*, *101*, 13,195–13,214. https://doi.org/10.1029/96JA00633

Anderson, B. J., Erlandson, R. E., & Zanetti, L. J. (1992). A statistical study of Pc 1–2 magnetic pulsations in the equatorial magnetosphere. I—Equatorial occurrence distributions. II—Wave properties. *Journal of Geophysical Research*, *97*, 3075–3101. https://doi.org/10.1029/91JA02706

Blum, L. W., MacDonald, E. A., Gary, S. P., Thomsen, M. F., & Spence, H. E. (2009). Ion observations from geosynchronous orbit as a proxy for ion cyclotron wave growth during storm times. *Journal of Geophysical Research*, *114*, A10214. https://doi.org/10.1029/2009JA014396

Bortnik, J., Cutler, J. W., Dunson, C., Bleier, T. E., & McPherron, R. L. (2008). *Journal of Geophysical Research*, *113*, A04201. https://doi.org/10.1029/2007JA012867

Bortnik, J., Thorne, R. M., & Omidi, N. (2010). Nonlinear evolution of EMIC waves in a uniform magnetic field: 2. Test-particle scattering. *Journal of Geophysical Research*, *115*, A12242. https://doi.org/10.1029/2010JA015603

Bossen, M., McPherron, R. L., & Russell, C. T. (1976). A statistical study of Pc 1 magnetic pulsations at synchronous orbit. *Journal of Geophysical Research*, *81*, 6083–6091. https://doi.org/10.1029/JA081i034p06083

Bräysy, T., Mursula, K., & Marklund, G. (1998). Ion cyclotron waves during a great magnetic storm observed by Freja double-probe electric field instrument. *Journal of Geophysical Research*, *103*, 4145–4156. https://doi.org/10.1029/97JA02820

Cornwall, J. M. (1965). Cyclotron instabilities and electromagnetic emission in the ultra low frequency and very low frequency ranges. *Journal of Geophysical Research*, *70*, 61–69. https://doi.org/10.1029/JZ070i001p00061

Denton, R. E., Anderson, B. J., Ho, G., & Hamilton, D. C. (1996). Effects of wave superposition on the polarization of electromagnetic ion cyclotron waves. *Journal of Geophysical Research*, *101*, 24,869–24,886. https://doi.org/10.1029/96JA02251

Denton, R. E., Hudson, M. K., & Roth, I. (1992). Loss-cone-driven ion cyclotron waves in the magnetosphere. *Journal of Geophysical Research*, *97*, 12,093–12,103. https://doi.org/10.1029/92JA00954

Engebretson, M. J., Lessard, M. R., Bortnik, J., Green, J. C., Horne, R. B., Detrick, D. L., et al. (2008). Pc1-Pc2 waves and energetic particle precipitation during and after magnetic storms: Superposed epoch analysis and case studies. *Journal of Geophysical Research*, *113*, A01211. https://doi.org/10.1029/2007JA012362

Engebretson, M. J., Peterson, W. K., Posch, J. L., Klatt, M. R., Anderson, B. J., Russell, C. T., et al. (2002). Observations of two types of Pc 1–2 pulsations in the outer dayside magnetosphere. *Journal of Geophysical Research*, *107*(A12), 1451. https://doi.org/10.1029/2001JA000198

Engebretson, M. J., Posch, J. L., Westerman, A. M., Otto, N. J., Slavin, J. A., Le, G., et al. (2008). Temporal and spatial characteristics of Pc1 waves observed by ST5. *Journal of Geophysical Research*, *113*, A07206. https://doi.org/10.1029/2008JA013145

Engebretson, M. J., Posch, J. L., Wygant, J. R., Kletzing, C. A., Lessard, M. R., Huang, C. L., et al. (2015). Van Allen probes, NOAA, GOES, and ground observations of an intense EMIC wave event extending over 12 h in magnetic local time. *Journal of Geophysical Research: Space Physics*, *120*, 5465–5488. https://doi.org/10.1002/2015JA021227

Erlandson, R. E., & Anderson, B. J. (1996). Pc 1 waves in the ionosphere: A statistical study. *Journal of Geophysical Research*, *101*, 7843–7858. https://doi.org/10.1029/96JA00082

Erlandson, R. E., & Ukhorskiy, A. J. (2001). Observations of electromagnetic ion cyclotron waves during geomagnetic storms: Wave occurrence and pitch angle scattering. *Journal of Geophysical Research*, *106*, 3883–3896. https://doi.org/10.1029/2000JA000083

Fraser, B. J., Grew, R. S., Morley, S. K., Green, J. C., Singer, H. J., Loto'aniu, T. M., & Thomsen, M. F. (2010). Storm time observations of electromagnetic ion cyclotron waves at geosynchronous orbit: GOES results. *Journal of Geophysical Research*, *115*, A05208. https://doi.org/10.1029/2009JA014516

Fraser, B. J., & Nguyen, T. S. (2001). Is the plasmapause a preferred source region of electromagnetic ion cyclotron waves in the magnetosphere? *Journal of Atmospheric and Terrestrial Physics*, *63*, 1225–1247. https://doi.org/10.1016/S1364-6826(00)00225-X

Halford, A. J., Fraser, B. J., & Morley, S. K. (2010). EMIC wave activity during geomagnetic storm and nonstorm periods: CRRES results. *Journal of Geophysical Research*, *115*, A12248. https://doi.org/10.1029/2010JA015716

Halford, A. J., Fraser, B. J., Morley, S. K., Elkington, S. R., & Chan, A. A. (2016). Dependence of EMIC wave parameters during quiet, geomagnetic storm, and geomagnetic storm phase times. *Journal of Geophysical Research: Space Physics*, *121*, 6277–6291. https://doi.org/10.1002/2016JA022694

He, F., Zhang, X.-X., Lin, R.-L., Fok, M.-C., Katus, R. M., Liemohn, M. W., et al. (2017). A new solar wind-driven global dynamic plasmapause model: 2. Model and validation. *Journal of Geophysical Research: Space Physics*, *122*, 7172–7187. https://doi.org/10.1002/2017JA023913

Heilig, B., & Lühr, H. (2018). Quantifying the relationship between the plasmapause and the inner boundary of small-scale field-aligned currents, as deduced from Swarm observations. *Annals of Geophysics*, *36*, 595–607. https://doi.org/10.5194/angeo-36-595-2018

Horne, R. B., & Thorne, R. M. (1993). On the preferred source location for the convective amplification of ion cyclotron waves. *Journal of Geophysical Research*, *98*, 9233–9247. https://doi.org/10.1029/92JA02972

Iyemori, T., & Hayashi, K. (1989). PC 1 micropulsations observed by Magsat in the ionospheric F region. *Journal of Geophysical Research*, *94*, 93–100. https://doi.org/10.1029/JA094iA01p00093

Johnson, J. R., & Cheng, C. Z. (1999). Can ion cyclotron waves propagate to the ground? *Geophysical Research Letters*, *26*, 671–674. https://doi.org/10.1029/1999GL900074

Jordanova, V. K., Farrugia, C. J., Thorne, R. M., Khazanov, G. V., Reeves, G. D., & Thomsen, M. F. (2001). Modeling ring current proton precipitation by electromagnetic ion cyclotron waves during the May 14–16, 1997, storm. *Journal of Geophysical Research*, *106*, 7–22. https://doi.org/10.1029/2000JA002008

Kasahara, Y., Sawada, A., Yamamoto, M., Kimura, I., Kokubun, S., & Hayashi, K. (1992). Ion cyclotron emissions observed by the satellite Akebono in the vicinity of the magnetic equator. *Radio Science*, *27*, 347–362. https://doi.org/10.1029/91RS01872

Keika, K., Takahashi, K., Ukhorskiy, A. Y., & Miyoshi, Y. (2013). Global characteristics of electromagnetic ion cyclotron waves: Occurrence rate and its storm dependence. *Journal of Geophysical Research: Space Physics*, *118*, 4135–4150. https://doi.org/10.1002/jgra.50385

Kim, H., Hwang, J., Park, J., Bortnik, J., & Lee, J. (2018). Global characteristics of electromagnetic ion cyclotron waves deduced from Swarm satellites. *Journal of Geophysical Research: Space Physics*, *123*, 1325–1336. https://doi.org/10.1002/2017JA024888

Kim, E.-H., & Johnson, J. R. (2016). Full-wave modeling of EMIC waves near the He^+ gyrofrequency. *Geophysical Research Letters*, *43*, 13–21. https://doi.org/10.1002/2015GL066978

Kim, H., Lessard, M. R., Engebretson, M. J., & Young, M. A. (2011). Statistical study of Pc1–2 wave propagation characteristics in the high-latitude ionospheric waveguide. *Journal of Geophysical Research*, *116*, A07227. https://doi.org/10.1029/2010JA016355

Kim, K.-H., Park, J.-S., Omura, Y., Shiokawa, K., Lee, D.-H., Kim, G.-J., et al. (2016). Spectral characteristics of steady quiet-time EMIC waves observed at geosynchronous orbit. *Journal of Geophysical Research: Space Physics*, *121*, 8640–8660. https://doi.org/10.1002/2016JA022957

Kletzing, C. A., Kurth, W. S., Acuna, M., MacDowall, R. J., Torbert, R. B., Averkamp, T., et al. (2013). The Electric and Magnetic Field Instrument Suite and Integrated Science (EMFISIS) on RBSP. *Space Science Reviews*, *179*, 127–181. https://doi.org/10.1007/s11214-013-9993-6

Kozyra, J. U., Cravens, T. E., Nagy, A. F., Fontheim, E. G., & Ong, R. S. B. (1984). Effects of energetic heavy ions on electromagnetic ion cyclotron wave generation in the plasmapause region. *Journal of Geophysical Research*, *89*, 2217–2233. https://doi.org/10.1029/JA089iA04p02217

Lee, J. H., & Angelopoulos, V. (2014). Observations and modeling of EMIC wave properties in the presence of multiple ion species as function of magnetic local time. *Journal of Geophysical Research: Space Physics*, *119*, 8942–8970. https://doi.org/10.1002/2014JA020469

Lee, D.-H., Johnson, J. R., Kim, K., & Kim, K.-S. (2008). Effects of heavy ions on ULF wave resonances near the equatorial region. *Journal of Geophysical Research*, *113*, A11212. https://doi.org/10.1029/2008JA013088

Liu, Y. H., Fraser, B. J., & Menk, F. W. (2012). Pc2 EMIC waves generated high off the equator in the dayside outer magnetosphere. *Geophysical Research Letters*, *39*, L17102. https://doi.org/10.1029/2012GL053082

Liu, Y. H., Fraser, B. J., Menk, F. W., Zhang, J. C., Kistler, L. M., & Dandouras, I. (2013). Correction to "Pc2 EMIC waves generated high off the equator in the dayside outer magnetosphere". *Geophysical Research Letters*, *40*, 1950–1951. https://doi.org/10.1002/grl.50283

Lühr, H., Park, J., Xiong, C., & Rauberg, J. (2014). Alfvén wave characteristics of equatorial plasma irregularities in the ionosphere derived from CHAMP observations. *Frontiers in Physics*, *2*, 47. https://doi.org/10.3389/fphy.2014.00047

Lühr, H., Xiong, C., Park, J., & Rauberg, J. (2014). Systematic study of intermediate-scale structures of equatorial plasma irregularities in the ionosphere based on CHAMP observations. *Frontiers in Physics*, *2*, 15. https://doi.org/10.3389/fphy.2014.00015

Lund, E. J., & LaBelle, J. (1997). On the generation and propagation of auroral electromagnetic ion cyclotron waves. *Journal of Geophysical Research*, *102*, 17,241–17,254. https://doi.org/10.1029/97JA01455

Lysak, RL., & Yoshikawa, A. (2013). Resonant cavities and waveguides in the ionosphere and atmosphere. In K. Takahashi, P. J. Chi, R. E. Denton, & R. L. Lysak (Eds.), *Magnetospheric ULF waves: Synthesis and new directions* (Vol. 169, pp. 289–306). American Geophysical Union.

McCollough, J. P., Elkington, S. R., & Baker, D. (2009). The role of Shabansky orbits in the generation of compression-related EMIC waves. AGU Fall Meeting Abstracts, SM43C-08.

McCollough, J. P., Elkington, S. R., & Baker, D. N. (2012). The role of Shabansky orbits in compression-related electromagnetic ion cyclotron wave growth. *Journal of Geophysical Research*, *117*, A01208. https://doi.org/10.1029/2011JA016948

McCollough, J. P., Elkington, S. R., Usanova, M. E., Mann, I. R., Baker, D. N., & Kale, Z. C. (2010). Physical mechanisms of compressional EMIC wave growth. *Journal of Geophysical Research*, *115*, A10214. https://doi.org/10.1029/2010JA015393

Meredith, N. P., Horne, R. B., Kersten, T., Fraser, B. J., & Grew, R. S. (2014). Global morphology and spectral properties of EMIC waves derived from CRRES observations. *Journal of Geophysical Research: Space Physics*, *119*, 5328–5342. https://doi.org/10.1002/2014JA020064

Min, K., Lee, J., Keika, K., & Li, W. (2012). Global distribution of EMIC waves derived from THEMIS observations. *Journal of Geophysical Research*, *117*, A05219. https://doi.org/10.1029/2012JA017515

Moldwin, M. B., Downward, L., Rassoul, H. K., Amin, R., & Anderson, R. R. (2002). A new model of the location of the plasmapause: CRRES results. *Journal of Geophysical Research*, *107*, 1339. https://doi.org/10.1029/2001JA009211

Morley, S. K., Ables, S. T., Sciffer, M. D., & Fraser, B. J. (2009). Multipoint observations of Pc1–2 waves in the afternoon sector. *Journal of Geophysical Research*, *114*, A09205. https://doi.org/10.1029/2009JA014162

Mursula, K., Blomberg, L. G., Lindqvist, P. A., Marklund, G. T., Braysy¨, T., Rasinkangas, R., & Tanskanen, P. (1994). Dispersive Pc1 bursts observed by Freja. *Geophysical Research Letters*, *21*, 1851–1854. https://doi.org/10.1029/94GL01584

Newell, P. T., Sotirelis, T., Liou, K., Meng, C. I., & Rich, F. J. (2007). A nearly universal solar wind-magnetosphere coupling function inferred from 10 magnetospheric state variables. *Journal of Geophysical Research*, *112*, A01206. https://doi.org/10.1029/2006JA012015

Park, J. S., Kim, K. H., Shiokawa, K., Lee, D. H., Lee, E., Kwon, H. J., & Jee, G. (2016). EMIC waves observed at geosynchronous orbit under quiet geomagnetic conditions Kp *le* 1. *Journal of Geophysical Research: Space Physics*, *121*, 1377–1390. https://doi.org/10.1002/2015JA021968

Park, J., Lühr, H., & Rauberg, J. (2013). Global characteristics of Pc1 magnetic pulsations during solar cycle 23 deduced from CHAMP data. *Annals of Geophysics*, *31*, 1507–1520. https://doi.org/10.5194/angeo-31-1507-2013

Perraut, S., Gendrin, R., Roux, A., & de Villedary, C. (1984). Ion cyclotron waves—Direct comparison between ground-based measurements and observations in the source region. *Journal of Geophysical Research*, *89*, 195–202. https://doi.org/10.1029/JA089iA01p00195

Rauch, J. L., & Roux, A. (1982). Ray tracing of ULF waves in a multicomponent magnetospheric plasma—Consequences for the generation mechanism of ion cyclotron waves. *Journal of Geophysical Research*, *87*, 8191–8198. https://doi.org/10.1029/JA087iA10p08191

Saikin, A. A., Jordanova, V. K., Zhang, J. C., Smith, C. W., Spence, H. E., Larsen, B. A., & Shprits, Y. Y. (2018). Comparing simulated and observed EMIC wave amplitudes using in situ Van Allen Probes' measurements. *Journal of Atmospheric and Terrestrial Physics*, *177*, 190–201. https://doi.org/10.1016/j.jastp.2018.01.024

Saikin, A. A., Zhang, J. C., Allen, R. C., Smith, C. W., Kistler, L. M., Spence, H. E., & Jordanova, V. K. (2015). The occurrence and wave properties of H^+-, He^+-, and O^+-band EMIC waves observed by the Van Allen Probes. *Journal of Geophysical Research: Space Physics*, *120*, 7477–7492. https://doi.org/10.1002/2015JA021358

Saikin, A. A., Zhang, J. C., Smith, C. W., Spence, H. E., Torbert, R. B., & Kletzing, C. A. (2016). The dependence on geomagnetic conditions and solar wind dynamic pressure of the spatial distributions of EMIC waves observed by the Van Allen Probes. *Journal of Geophysical Research: Space Physics*, *121*, 4362–4377. https://doi.org/10.1002/2016JA022523

Shabansky, V. P. (1971). Some processes in the magnetosphere. *Space Science Reviews*, *12*, 299–418. https://doi.org/10.1007/BF00165511

Thorne, R. M., & Horne, R. B. (1997). Modulation of electromagnetic ion cyclotron instability due to interaction with ring current O^+ during magnetic storms. *Journal of Geophysical Research*, *102*, 14,155–14,164. https://doi.org/10.1029/96JA04019

Thorne, R. M., & Kennel, C. F. (1971). Relativistic electron precipitation during magnetic storm main phase. *Journal of Geophysical Research*, *76*, 4446. https://doi.org/10.1029/JA076i019p04446

Tsyganenko, N. A. (1995). Modeling the Earth's magnetospheric magnetic field confined within a realistic magnetopause. *Journal of Geophysical Research*, *100*, 5599–5612. https://doi.org/10.1029/94JA03193

Tsyganenko, N. A. (1996). Effects of the solar wind conditions in the global magnetospheric configurations as deduced from data-based field models (Invited). In E J. Rolfe & B. Kaldeich (Eds.), *International Conference on Substorms* (Vol. 389, pp. 181). ESA Special Publication.

Usanova, M. E., Darrouzet, F., Mann, I. R., & Bortnik, J. (2013). Statistical analysis of EMIC waves in plasmaspheric plumes from Cluster observations. *Journal of Geophysical Research: Space Physics*, *118*, 4946–4951. https://doi.org/10.1002/jgra.50464

Usanova, M. E., Mann, I. R., Bortnik, J., Shao, L., & Angelopoulos, V. (2012). THEMIS observations of electromagnetic ion cyclotron wave occurrence: Dependence on AE, SYMH, and solar wind dynamic pressure. *Journal of Geophysical Research*, *117*, A10218. https://doi.org/10.1029/2012JA018049

Wang, X. Y., Huang, S. Y., Allen, R. C., Fu, H. S., Deng, X. H., Zhou, M., & Torbert, R. B. (2017). The occurrence and wave properties of EMIC waves observed by the Magnetospheric Multiscale (MMS) mission. *Journal of Geophysical Research: Space Physics*, *122*, 8228–8240. https://doi.org/10.1002/2017JA024237

Wang, D., Yuan, Z., Yu, X., Deng, X., Zhou, M., Huang, S., & Wygant, J. R. (2015). Statistical characteristics of EMIC waves: Van Allen Probe observations. *Journal of Geophysical Research: Space Physics*, *120*, 4400–4408. https://doi.org/10.1002/2015JA021089

Wang, D., Yuan, Z., Yu, X., Huang, S., Deng, X., Zhou, M., & Li, H. (2016). Geomagnetic storms and EMIC waves: Van Allen Probe observations. *Journal of Geophysical Research: Space Physics*, *121*, 6444–6457. https://doi.org/10.1002/2015JA022318

Wild, C. J., & Seber, G. A. (2000). The Wilcoxon rank-sum test. In C. Encount (Ed.), *A first course data anal. inference* (pp. 611). New York: John Wiley and Sons.

Young, D. T., Perraut, S., Roux, A., de Villedary, C., Gendrin, R., Korth, A., & Jones, D. (1981). Wave-particle interactions near Omega/He plus/ observed on GEOS 1 and 2. I—Propagation of ion cyclotron waves in He/plus/-rich plasma. *Journal of Geophysical Research*, *86*, 6755–6772. https://doi.org/10.1029/JA086iA08p06755

Yu, X., Yuan, Z., Wang, D., Li, H., Huang, S., Wang, Z., & Wygant, J. R. (2015). In situ observations of EMIC waves in O^+ band by the Van Allen Probe A. *Geophysical Research Letters*, *42*, 1312–1317. https://doi.org/10.1002/2015GL063250